J Biomol NMR (2011) 50:167–190
DOI 10.1007/s10858-011-9507-3

ARTICLE

Improved accuracy in measuring one-bond and two-bond $^{15}N,^{13}C^{\alpha}$ coupling constants in proteins by double-inphase/antiphase (DIPAP) spectroscopy

Frank Löhr · Sina Reckel · Susanne Stefer · Volker Dötsch · Jürgen M. Schmidt

Received: 28 February 2011 / Accepted: 25 April 2011 / Published online: 7 June 2011

Abstract An extension to HN(CO-α/β-N,C^{α}-*J*)-TROSY (Permi and Annila in J Biomol NMR 16:221–227, 2000) is proposed that permits the simultaneous determination of the four coupling constants $^{1}J_{N'(i)C\alpha(i)}$, $^{2}J_{HN(i)C\alpha(i)}$, $^{2}J_{C\alpha(i-1)N'(i)}$, and $^{3}J_{C\alpha(i-1)HN(i)}$ in $^{15}N,^{13}C$-labeled proteins. Contrasting the original scheme, in which two separate subspectra exhibit the $^{2}J_{C\alpha N'}$ coupling as inphase and antiphase splitting (IPAP), we here record four subspectra that exhibit all combinations of inphase and antiphase splittings possible with respect to both $^{2}J_{C\alpha N'}$ and $^{1}J_{N'C\alpha}$ (DIPAP). Complementary sign patterns in the different spectrum constituents overdetermine the coupling constants which can thus be extracted at higher accuracy than is possible with the original experiment. Fully exploiting data redundancy, simultaneous 2D lineshape fitting of the E.COSY multiplet tilts in all four subspectra provides all coupling constants at ultimate precision. Cross-correlation and differential-relaxation effects were taken into account in the evaluation procedure. By applying a four-point Fourier transform, the set of spectra is reversibly interconverted between DIPAP and spin-state representations. Methods are exemplified using proteins of various size.

Keywords Correlation · Fourier transform · Heteronuclear coupling constant · Multiplet simulation · Protein structure · Spin-state editing · Ubiquitin · Ribonuclease T1 · Xylanase · Get2 domain · Proteorhodopsin

Dedicated to Professor Heinz Rüterjans on the occasion of his 75th birthday.

Electronic supplementary material The online version of this article (doi:10.1007/s10858-011-9507-3) contains supplementary material, which is available to authorized users.

F. Löhr (✉) · S. Reckel · S. Stefer · V. Dötsch
Institute of Biophysical Chemistry, Center for Biomolecular Magnetic Resonance, Goethe-University, Max-von-Laue-Str. 9, 60438 Frankfurt am Main, Germany
e-mail: murph@bpc.uni-frankfurt.de

J. M. Schmidt (✉)
School of Biosciences, University of Kent, Giles Lane, Canterbury, Kent CT2 7NJ, UK
e-mail: j.m.schmidt@kent.ac.uk

Introduction

Several one-bond and two-bond NMR coupling constants in polypeptides exhibit significant dependences on molecular conformation (Delaglio et al. 1991; Edison et al. 1994a, b; Wirmer and Schwalbe 2002; Liu and Prestegard 2009; Schmidt et al. 2009, 2010) and were recently utilised in a *J*-coupling index approach to annotating protein secondary-structure motifs (Schmidt et al. 2011). The three most promising heteronuclear coupling types, $^{2}J_{C\alpha(i-1)N'(i)}$, $^{1}J_{N'(i)C\alpha(i)}$, and $^{2}J_{HN(i)C\alpha(i)}$, can be measured in a single NMR experiment conveniently correlating the amide spins $^{15}N'$ and $^{1}H^{N}$ of residue *i* in the polypeptide backbone of uniformly $^{15}N,^{13}C$-isotope-labeled proteins (Permi and Annila 2000). Simultaneous scalar couplings from the pair of $^{13}C^{\alpha}$ nuclei of two successive amino-acid residues to the intervening ^{15}N nucleus results in a doublet of doublets in the ^{15}N spectrum dimension. If the C^{α} spin states are preserved between the chemical-shift evolution periods, the E.COSY mode allows also to extract the small associated couplings from the ^{1}H dimension. In decoupled mode, this spin topology is often exploited in triple-resonance NMR experiments for obtaining sequential resonance assignments (Fig. 1).

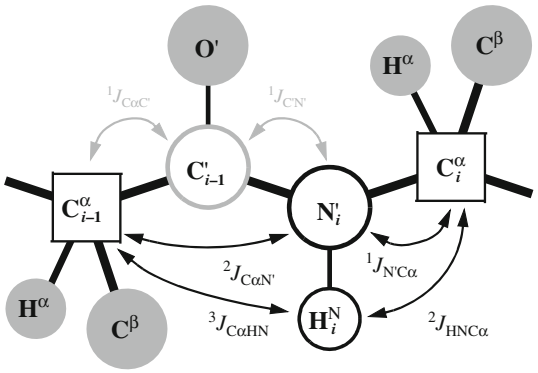

Fig. 1 Generic amino-acid mainchain fragment identifying coupling constants accessible in standard and double-IPAP variants of the HN(CO-α/β-NC$^\alpha$-*J*) experiment. Linked by two auxiliary couplings, the carbonyl carbon serves as a magnetization-relay spin and enables discrimination of both C$^\alpha$ sites. *Squares* indicate passive spins giving rise to E.COSY-type splittings

At any rate, the two C$^\alpha$ spins are distinguished by their coupling pathways to the ^{15}N spin, where the directly bonded C^α_i is coupled via the one-bond interaction $^1J_{N'C\alpha}$, and the remote C^α_{i-1} is coupled via both the two-bond interaction $^2J_{C\alpha N'}$ and the two one-bond interactions $^1J_{N'C'}$ and $^1J_{C'C\alpha}$. Reminiscent of the intra-HNCA experiment (Brutscher 2002; Nietlispach et al. 2002; Permi 2002), distinction between inter- and intra-residual connectivity is thus accomplished by the exclusive presence of the carbonyl spin in the two-bond coupling path between N′ of the current and C$^\alpha$ of the preceding amino acid.

Magnitudes of $^2J_{C\alpha(i-1)N'(i)}$ and $^1J_{N'(i)C\alpha(i)}$ correlate primarily with torsion angles ψ_{i-1} and ϕ_i, respectively, suggesting that their measurement is useful to determining protein backbone conformation. Yet, obtaining accurate *J* values in larger proteins poses certain challenges. The fact that both *J*-coupling interactions are of similar type and magnitude complicates their quantitative evaluation (Fig. 2).

Both $^1J_{N'C\alpha}$ and $^2J_{C\alpha N'}$ coupling constants can be extracted from [^{15}N,^{1}H]-HSQC spectra when decoupling exclusively ^{13}C′ while preserving ^{13}C$^\alpha$ spin states (Delaglio et al. 1991), albeit only under favourable conditions (narrow lines, large and significantly different values of *J*).

A variety of other methods have been proposed to resolve or avoid interference between one-bond and two-bond couplings, such as the frequency-based inphase/antiphase (IPAP) pulse scheme by Permi and Annila (2000). Amplitude-based schemes comprise *J*-modulation (Wirmer and Schwalbe 2002), TROSY-based *J*-modulation in conjunction with computer-optimization of one- and two-bond N–C coupling parameters measured in large proteins (Liu and Prestegard 2009), and quantitative *J*-correlation (Wienk et al. 2003).

Should the size of the two-bond coupling $^2J_{C\alpha N'}$ exceed that of the one-bond coupling $^1J_{N'C\alpha}$, ambiguity would arise with the *J*-modulation approach, which cannot discriminate this situation, and data evaluations ordinarily rely on the assumption that both couplings are 3 Hz apart.

Aimed at measuring $^2J_{C\alpha N'}$, $^1J_{N'C\alpha}$, and $^1J_{C'N'}$ simultaneously, the drawback of quantitative *J*-correlation is that signal amplitudes depend on all three coupling constants, values of which are grouped around 7.7, 10.7, and 15.0 Hz, respectively. Each signal emerges with a sine dependence on the respective active coupling which evolves over a critical magnetization transfer period, however, both other passive couplings attenuate the signal according to their cosine dependences, implying inherent intensity loss. Encoding coupling information in the signal amplitude, quantitative *J*-correlation is complementary to the frequency-encoded E.COSY-type approach suggested in the present work.

Permi and Annila (2000) recorded IP and AP subspectra with respect to one of both N′,C$^\alpha$ splittings and resolved the two-bond coupling in the presence of broad lines. However, as the IP/AP set refers exclusively to the two-

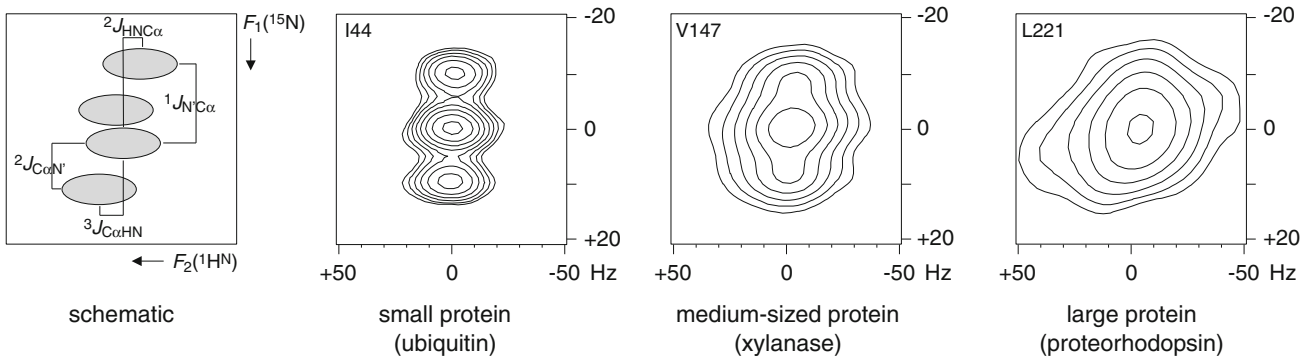

Fig. 2 Schematic and experimental E.COSY-type multiplet patterns seen in ^{13}C$^\alpha$-coupled, ^{13}C′-decoupled [^{15}N,^{1}H]-BIRD-TROSY spectra. The individual multiplet lines lose resolution with increasing molecular weight and molecular rotational correlation time. Examples recorded at 500, 800, and 950 MHz, respectively, show signals from ubiquitin, xylanase, and proteorhodopsin which exhibit τ_c values of 4.1, 13, and 23 ns, and typical ^{15}N linewidths of 3.5 Hz, 8 Hz, and 12 Hz

bond connectivity, only this smaller value of $^{2}J_{C\alpha N'}$ is extracted with high accuracy and precision, while that of the larger one-bond coupling $^{1}J_{N'C\alpha}$ derives only from an inphase splitting, with no supporting complementary antiphase pattern, and is therefore more exposed to covariance effects.

Extending the approach by Permi and Annila, we here propose a double-IPAP (DIPAP) concept in order to resolve the one-bond coupling $^{1}J_{N'C\alpha}$ as accurately as the $^{2}J_{C\alpha N'}$ coupling. Our modular pulse-sequence scheme, termed [^{15}N,^{1}H]-TROSY-HN(CO-α/β-NC$^{\alpha}_{i,i-1}$-*J*)-DIPAP features unambiguous separation and extraction of all four individual ^{15}N,^{1}H cross-peak components with respect to the four possible combinations of $^{13}C^{\alpha}_{i}$ and $^{13}C^{\alpha}_{i-1}$ spin states and, thus, permits the determination of the four polypeptide coupling constants $^{1}J_{N'(i)C\alpha(i)}$, $^{2}J_{C\alpha(i-1)N'(i)}$, $^{2}J_{HN(i)C\alpha(i)}$, and $^{3}J_{C\alpha(i-1)HN(i)}$. In the following, we omit the amino-acid residue indeces when ambiguity cannot arise. The technology will benefit especially the coupling analysis in the presence of broad ^{15}N resonance lines typical of larger protein molecules with prolonged reorientational correlation times.

Methods

Pulse sequence description

Even though ^{15}N linewidths may be considerably smaller than the coupling constants, the two central lines of the N′,C$^{\alpha}$,C$^{\alpha}$ doublet of doublets tend to overlap, precluding accurate measurement (Fig. 2). The [^{15}N,^{1}H]-TROSY-HN(CO-α/β-NC$^{\alpha}$-*J*) experiment by Permi and Annila (2000) exploits the spin topology in the peptide bond comprising the couplings $^{1}J_{C'N'}$, $^{1}J_{C\alpha C'}$, $^{2}J_{C\alpha N'}$, and $^{1}J_{N'C\alpha}$ (Fig. 1) and, in an IPAP manner, discriminates the two similarly sized ^{15}N,^{13}C$^{\alpha}$ splittings by separating into two subspectra only those doublet components associated with $^{2}J_{C\alpha N'}$. In larger proteins, the ill-resolved inphase doublet with respect to $^{13}C^{\alpha}_{i}$ would prevent accurate determination of $^{1}J_{N'C\alpha}$, and the associated $^{2}J_{HNC\alpha}$ coupling altogether.

Our novel [^{15}N,^{1}H]-TROSY-HN(CO-α/β-NC$^{\alpha}_{i,i-1}$-*J*)-DIPAP pulse sequence (Fig. 3) provides separation of all four multiplet lines. This is achieved by alternately refocusing (**a**) and evolving (**b**) both ^{15}N,^{13}C$^{\alpha}$ interactions during an interval δ, which is concatenated with a period ζ for the build-up of ^{15}N antiphase magnetization with respect to ^{13}C′, followed by alternately refocusing (**c**) and evolving (**d**) the $^{1}J_{C\alpha C'}$ coupling during period ε. Pairwise combinations of the pulse-sequence modules **a**–**d** then permit the extraction of both $^{1}J_{N'C\alpha}$ and $^{2}J_{C\alpha N'}$ from the F_1(^{15}N) spectrum dimension, and of $^{2}J_{HNC\alpha}$ and $^{3}J_{C\alpha HN}$ from F_2(^{1}H).

In **module a**, refocusing of both N′,C$^{\alpha}$ couplings leads, after periods δ and ζ, to $N'_yC'_z$ magnetization exclusively. In contrast, evolution of both N′,C$^{\alpha}$ couplings during δ in **module b** generates the four terms:

$$\begin{aligned} M(\delta) = &- 2N'_xC'_z \cos\left(^{1}J_{N'C\alpha}\pi\delta\right)\cos\left(^{2}J_{C\alpha N'}\pi\delta\right) \\ &- 4N'_yC'_zC^{\alpha(i)}_z \sin\left(^{1}J_{N'C\alpha}\pi\delta\right)\cos\left(^{2}J_{C\alpha N'}\pi\delta\right) \\ &- 4N'_yC'_zC^{\alpha(i-1)}_z \cos\left(^{1}J_{N'C\alpha}\pi\delta\right)\sin\left(^{2}J_{C\alpha N'}\pi\delta\right) \\ &+ 8N'_xC'_zC^{\alpha(i)}_zC^{\alpha(i-1)}_z \sin\left(^{1}J_{N'C\alpha}\pi\delta\right)\sin\left(^{2}J_{C\alpha N'}\pi\delta\right) \end{aligned} \quad (1)$$

The phase cycle ϕ_2 eliminates the N'_y components, however, a distinction between the N'_x components cannot be made, and both terms are retained and superimpose in the same multiplet. An appropriate choice of δ will make the amplitude factor $\cos(^{1}J_{N'C\alpha}\pi\delta)\cos(^{2}J_{C\alpha N'}\pi\delta)$ small compared to $\sin(^{1}J_{N'C\alpha}\pi\delta)\sin(^{2}J_{C\alpha N'}\pi\delta)$.

In **module c**, the two C$^{\alpha}$-selective inversion pulses have no net effect on those terms containing none or both C$^{\alpha}$ operators, $N'_yC'_z$ and $N'_yC'_zC^{\alpha(i)}_zC^{\alpha(i-1)}_z$, to the effect that the carbonyl inversion pulse refocuses all C',C$^{\alpha}$ couplings, including primarily $^{1}J_{C\alpha C'}$, and also $^{2}J_{C'C\alpha} \approx -0.6 \pm 0.3$ Hz (Schmidt et al. 2010).

In **module d**, coupling does evolve between the carbonyl spin $^{13}C'_{i-1}$ and its directly bonded carbon $^{13}C^{\alpha}_{i-1}$, converting the term $2N'_xC'_z$ originating from module **a** into $-4N'_yC'_zC^{\alpha(i-1)}_z$ and the term $8N'_xC'_zC^{\alpha(i)}_zC^{\alpha(i-1)}_z$ originating from module **b** into $-4N'_yC'_zC^{\alpha(i)}_z$.

Depending on the combination of building blocks **a**–**d**, the terms obtained prior to ^{15}N evolution are as follows:

$$(\mathbf{a}+\mathbf{c}) \rightarrow \quad M_{II}(\delta,\varepsilon) = +2N'_yC'_z \sin(^{1}J_{N'C'}\pi\zeta) \quad (2a)$$

$$(\mathbf{b}+\mathbf{c}) \rightarrow \quad M_{AA}(\delta,\varepsilon) = +8N'_yC'_zC^{\alpha(i)}_zC^{\alpha(i-1)}_z \sin(^{1}J_{N'C'}\pi\zeta)\sin(^{1}J_{N'C\alpha}\pi\delta)\sin(^{2}J_{C\alpha N'}\pi\delta) \quad (2b)$$

$$(\mathbf{a}+\mathbf{d}) \rightarrow \quad M_{IA}(\delta,\varepsilon) = -4N'_yC'_zC^{\alpha(i-1)}_z \sin(^{1}J_{N'C'}\pi\zeta)\sin(^{1}J_{C'C\alpha}\pi\varepsilon) \quad (2c)$$

$$(\mathbf{b}+\mathbf{d}) \rightarrow \quad M_{AI}(\delta,\varepsilon) = -4N'_yC'_zC^{\alpha(i)}_z \sin(^{1}J_{N'C'}\pi\zeta)\sin(^{1}J_{C'C\alpha}\pi\varepsilon)\sin(^{1}J_{N'C\alpha}\pi\delta)\sin(^{2}J_{C\alpha N'}\pi\delta) \quad (2d)$$

^{15}N chemical shifts as well as one-bond and two-bond ^{15}N–^{13}C$^{\alpha}$ couplings evolve in the subsequent semi-constant time period as a function of t_1, while ^{15}N antiphase magnetization with respect to ^{13}C' refocuses during the fixed duration $T_N = \zeta = (2\ ^{1}J_{C'N'})^{-1}$. The final ST2-PT

element (Pervushin et al. 1998) provides detectable proton magnetization which, under the couplings $^2J_{\mathrm{HNC}\alpha}$ and $^3J_{\mathrm{C}\alpha\mathrm{HN}}$, evolves during acquisition time t_2.

Substituting polarization operators for longitudinal magnetization z-components of the passive spins,

$$\begin{aligned} C_{|\alpha\rangle}^{\alpha(i)} &= 1/2 + \mathrm{C}_z^{\alpha(i)}, \\ C_{|\beta\rangle}^{\alpha(i)} &= 1/2 - \mathrm{C}_z^{\alpha(i)}, \\ C_{|\alpha\rangle}^{\alpha(i-1)} &= 1/2 + \mathrm{C}_z^{\alpha(i-1)}, \\ C_{|\beta\rangle}^{\alpha(i-1)} &= 1/2 - \mathrm{C}_z^{\alpha(i-1)}, \end{aligned} \tag{3}$$

with composite frequencies for both chemical-shift and coupling terms in the F_1 dimension,

$$\begin{aligned} |\alpha\rangle_1^{(i)} &= \omega_{\mathrm{N}'} + \pi\,{}^1J_{\mathrm{N}'\mathrm{C}\alpha}, \\ |\beta\rangle_1^{(i)} &= \omega_{\mathrm{N}'} - \pi\,{}^1J_{\mathrm{N}'\mathrm{C}\alpha}, \\ |\alpha\rangle_1^{(i-1)} &= \omega_{\mathrm{N}'} + \pi\,{}^2J_{\mathrm{C}\alpha\mathrm{N}'}, \\ |\beta\rangle_1^{(i-1)} &= \omega_{\mathrm{N}'} - \pi\,{}^2J_{\mathrm{C}\alpha\mathrm{N}'}, \end{aligned} \tag{4}$$

and likewise for the F_2 dimension,

$$\begin{aligned} |\alpha\rangle_2^{(i)} &= \omega_{\mathrm{HN}} + \pi\,{}^2J_{\mathrm{HNC}\alpha}, \\ |\beta\rangle_2^{(i)} &= \omega_{\mathrm{HN}} - \pi\,{}^2J_{\mathrm{HNC}\alpha}, \\ |\alpha\rangle_2^{(i-1)} &= \omega_{\mathrm{HN}} + \pi\,{}^3J_{\mathrm{C}\alpha\mathrm{HN}}, \\ |\beta\rangle_2^{(i-1)} &= \omega_{\mathrm{HN}} - \pi\,{}^3J_{\mathrm{C}\alpha\mathrm{HN}}, \end{aligned} \tag{5}$$

the observable magnetization giving rise to the 2D multiplet located at coordinates ($\omega_{\mathrm{N}'}$,ω_{HN}) comprises 16 individual lines whose superposition generates the double E.COSY-type multiplet patterns (Griesinger et al. 1987) depicted in Fig. 4.

Addressing the coupling pair sorted as $^1J_{\mathrm{N}'\mathrm{C}\alpha}/^2J_{\mathrm{C}\alpha\mathrm{N}'}$, the shorthand for naming the four separable DIPAP spectrum constituents shall parallel the order of the pulse sequence events where, first, module **a** or **b** determines the splitting pattern with respect to ^1J and, second, module **c** or **d** determines the pattern with respect to ^2J. Thus, IA = M_{IA} = IP(^1J)AP(^2J) denotes the pattern exhibiting splittings inphase with respect to ^1J and antiphase with respect to ^2J, and likewise for the other three constituents.

Resolution enhancements

The BIRD pulse-sequence element (Garbow et al. 1982; Uhrín et al. 1993; Emetarom et al. 1995) had previously been applied to the measurement of $^1J_{\mathrm{C}'\mathrm{N}'}$ (Kövér and Batta 2004), but not, to our knowledge, to the measurement of $J_{\mathrm{C}\alpha\mathrm{N}'}$. Its purpose is the avoidance of unwanted splittings that would otherwise increase the ^{15}N linewidth. Acting as a π inversion pulse selective to ^{1}H not bonded to ^{15}N, the BIRD element affects the ^{15}N dimension only. Less beneficial, perhaps, to more sizeable proteins, it eliminates the usually unresolved small splittings due to $^2J_{\mathrm{N}'\mathrm{H}\alpha}$, $^3J_{\mathrm{N}'\mathrm{H}\beta}$, and $^3J_{\mathrm{H}\alpha\mathrm{N}'}$ without interfering with the TROSY effect.

Experiments using BIRD trade sensitivity for improved resolution. Chiefly because of the added 10.8-ms period during which ^{1}H transverse magnetization prevails and

Fig. 3 Pulse sequence of the [^{15}N,^{1}H]-TROSY-HN(CO-α/β-NC$^{\alpha}_{i,i-1}$-J)-DIPAP experiment: *scheme A* conventional (non-selective) and *scheme B* BEST (longitudinal relaxation optimized, Schanda et al. 2006; Lescop et al. 2010) version. Alternative insertion of modules **a** or **b** and **c** or **d** in interleaved records yields four possible $^1J_{\mathrm{NC}\alpha}/^2J_{\mathrm{C}\alpha\mathrm{N}}$ splitting patterns: (a + c) IP/IP, (b + d) AP/IP, (b + c) AP/AP, and (a + d) IP/AP. Filled and open symbols represent RF-pulse flip angles of 90° and 180°, respectively. Rectangular proton and nitrogen pulses use the highest available power level. In *scheme A*, proton pulses are applied at the water resonance. Gaussian shaped 90° ^{1}H pulses (1.5 ms duration, 10% truncation level) align the water magnetization along the positive z axis to avoid saturation of fast exchanging amide protons (Grzesiek and Bax 1993a; Stonehouse et al. 1994; Matsuo et al. 1996), except the second and third Gaussian pulse use 4 ms to minimize perturbation of ^{1}H$^{\alpha}$ spins during the G-BIRD$_r$ element (Garbow et al. 1982; Uhrín et al. 1993; Emetarom et al. 1995; Kövér and Batta 2004). Proton pulse widths given in the following for *scheme B* are valid for 600 MHz Larmor frequency and scale with 600/X for applications carried out at X-MHz spectrometers. The pair of 2-ms I-BURP-2 pulses (Geen and Freeman 1991), applied at an offset of 2.8 ppm, refocuses ^{15}N–^{1}H$^{\alpha}$ and ^{15}N–^{1}H$^{\beta}$ long-range interactions during ^{15}N evolution. All other ^{1}H pulses apply to the amide proton region (at ca. 8.3 ppm). The 180° ^{1}H pulses (2 ms duration) during periods τ employ the RE-BURP shape (Geen and Freeman 1991). The first two 90° ^{1}H pulses (3 ms) have PC9 shapes (Kupče and Freeman 1994), the remaining two (1.92 ms) employ E-BURP-2 (Geen and Freeman 1991), the first one has a time-reversed amplitude profile. Carbonyl-selective 90° and 180° ^{13}C pulses have 150 µs durations and shapes correspond to the center lobe of a sin(x)/x function. Band-selective decoupling during acquisition using 3-ms WURST-20 pulses (Kupče and Freeman 1995) with 15 kHz sweep eliminates line-broadening due to two- and three-bond ^{13}C'–^{1}H$^{\mathrm{N}}$ couplings. Inversion pulses applied to α-carbons employ an RF field of $\Delta\nu/3^{1/2}$, with $\Delta\nu$ the frequency difference between the centers of the ^{13}C$^{\alpha}$ and ^{13}C' spectral regions (Kay et al. 1990). Unspecified RF-pulse phases default to x. Phase cycling is ϕ_1 = 2(y), 2(−y); $\phi_2 = -\phi_1$; ϕ_3 = x, −x; ϕ_4 = y, −y; ϕ_5 = 4(x), 4(−x); ϕ_6 = y; ϕ_7 = x; ϕ_{rec} = x, 2(−x), x, −x, 2(x), −x. Applied along the z-axis, sine-bell shaped field gradients use the following durations and peak amplitudes (percentage of the maximum available gradient strength, ca. 70 G/cm): G$_1$, 0.5 ms, −10%; G$_2$, 0.5 ms, −15%; G$_3$, 0.5 ms, +12%; G$_4$, 0.5 ms, +14%; G$_5$, 0.175 ms, −78.9%; G$_6$, 0.5 ms, +11%; G$_7$, 1.05 ms, −78.9%; G$_8$, 0.3 ms, +8%; G$_9$, 0.8 ms, +25%; G$_{10}$, 0.175 ms, +64%. In *scheme B*, G$_5$ and G$_7$ combine into a single 1.4-ms gradient of +78.9% amplitude. The semi-constant-time ^{15}N shift evolution (Logan et al. 1992; Grzesiek and Bax 1993b) uses parameter $\chi = T_{\mathrm{N}}/t_{1\mathrm{max}}$. For each t_1 increment, N- and P-type transients are collected alternately by inverting the polarity of G$_5$ and G$_7$ along with pulse phases ϕ_6 and ϕ_7, and stored separately. Both FIDs added and subtracted, with a 90° zero-order phase applied to one of the components, form real and imaginary parts of a complex data point. Pulse phase ϕ_5 and ϕ_{rec} inverted in every other t_1 increment shift axial peaks to the spectrum edge in the ^{15}N dimension. Fixed delays are τ = 4.6 ms; $\zeta = T_{\mathrm{N}}$ = 33 ms ≈ $(2^1J_{\mathrm{N}'\mathrm{C}'})^{-1}$; δ = 48 ms ≈ $(2^1J_{\mathrm{N}'\mathrm{C}\alpha})^{-1}$; ε = 9.2 ms ≈ $(2^1J_{\mathrm{C}'\mathrm{C}\alpha})^{-1}$; τ' = 5.4 ms ≈ $(2^1J_{\mathrm{N}'\mathrm{HN}})^{-1}$; τ_{G} = 0.36 ms (includes gradient duration and recovery time)

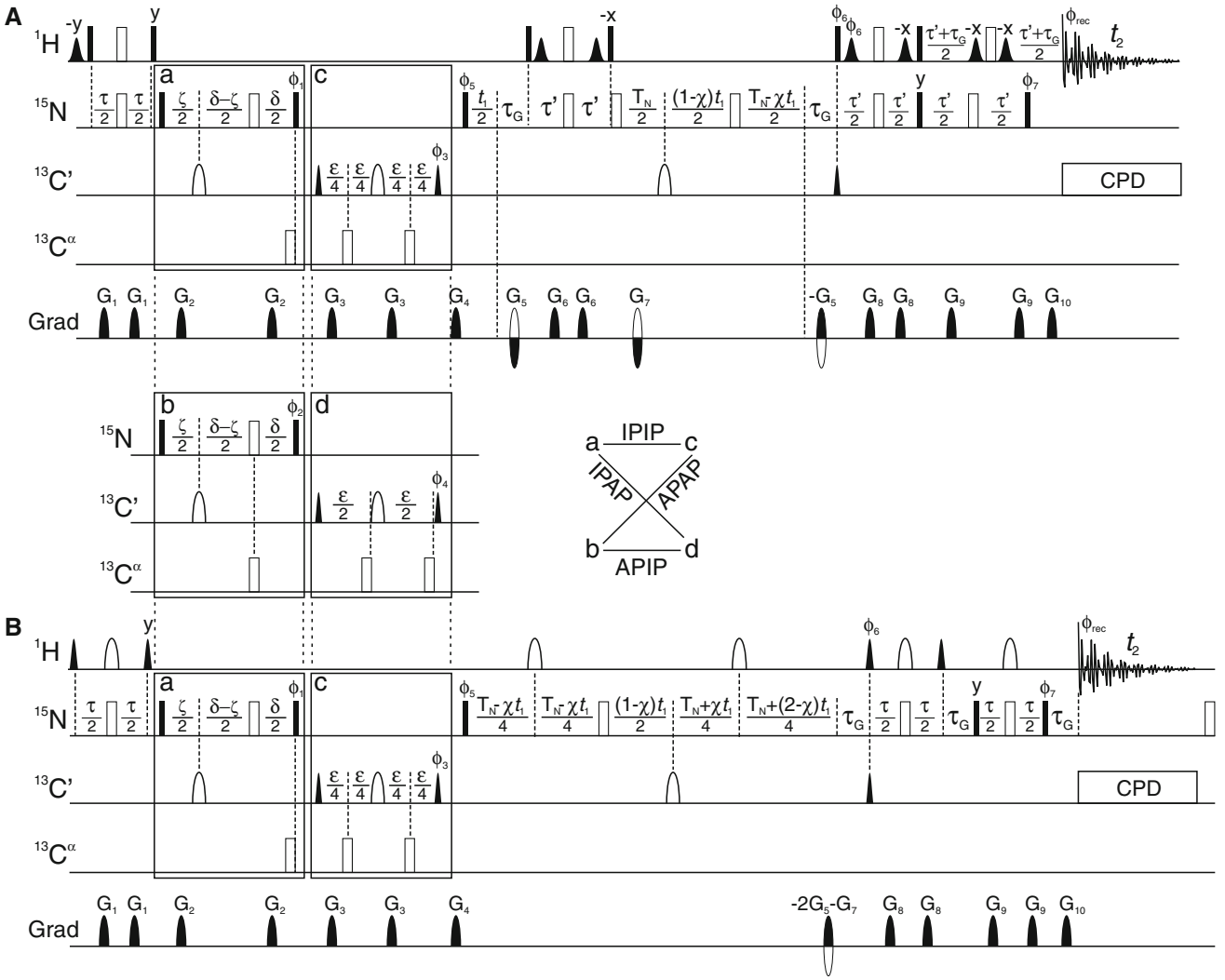

relaxation can take place, spectra typically exhibit a lower S/N ratio. Alternatively, a BEST-type pulse sequence (Fig. 3b) (Schanda et al. 2006; Lescop et al. 2010) can be used when ^{1}H shift spreads are narrow. Differing from its original intention of shortening experiment time, our motivation of applying the BEST concept is to improve sensitivity rather. Here, the pair of band-selective ^{1}H inversion pulses applied to the center of $^{1}H^{\alpha/\beta}$ chemical-shift region is employed to suppress evolution of ^{15}N–^{1}H long-range couplings during t_1, in order to avoid multiplet line distortion caused by unresolved E.COSY effects involving $^{3}J_{HNH\alpha}$ and $^{2}J_{N'H\alpha}$ and to reduce relaxation originating from N′–C^{α},N′–$H^{\alpha/\beta}$ dipole–dipole interference (Yao et al. 2009).

Fully deuterated samples, however, do not require the BIRD element or any band-selective ^{1}H inversion pulses if sensitivity is to be maximized.

The ^{15}N-180° pulse applied following ^{1}H acquisition enhances sensitivity as well as resolution along the ^{15}N dimension due to constructive addition of polarization from proton magnetization longitudinally relaxed during the pulse sequence and (subsequently) transferred to ^{15}N by the ST2-PT element (Favier and Brutscher 2011).

Experimental section

Protein samples

Ubiquitin

Measurements on 76-residue human ubiquitin used primarily a recombinant uniformly ^{13}C,^{15}N-doubly labeled sample dissolved at 1 mM concentration in 50 mM HEPES (pH 7). Investigations into differential-relaxation effects also used ^{2}H(70%),^{13}C,^{15}N-triply labeled ubiquitin (purchased as "99%"-^{2}H from VLI Research Inc., Malvern, PA) concentrated at 1.2 mM in 50 mM potassium phosphate buffer (pH 6). The aqueous solutions contained 10% D_2O. The temperature was 298 K in all NMR experiments.

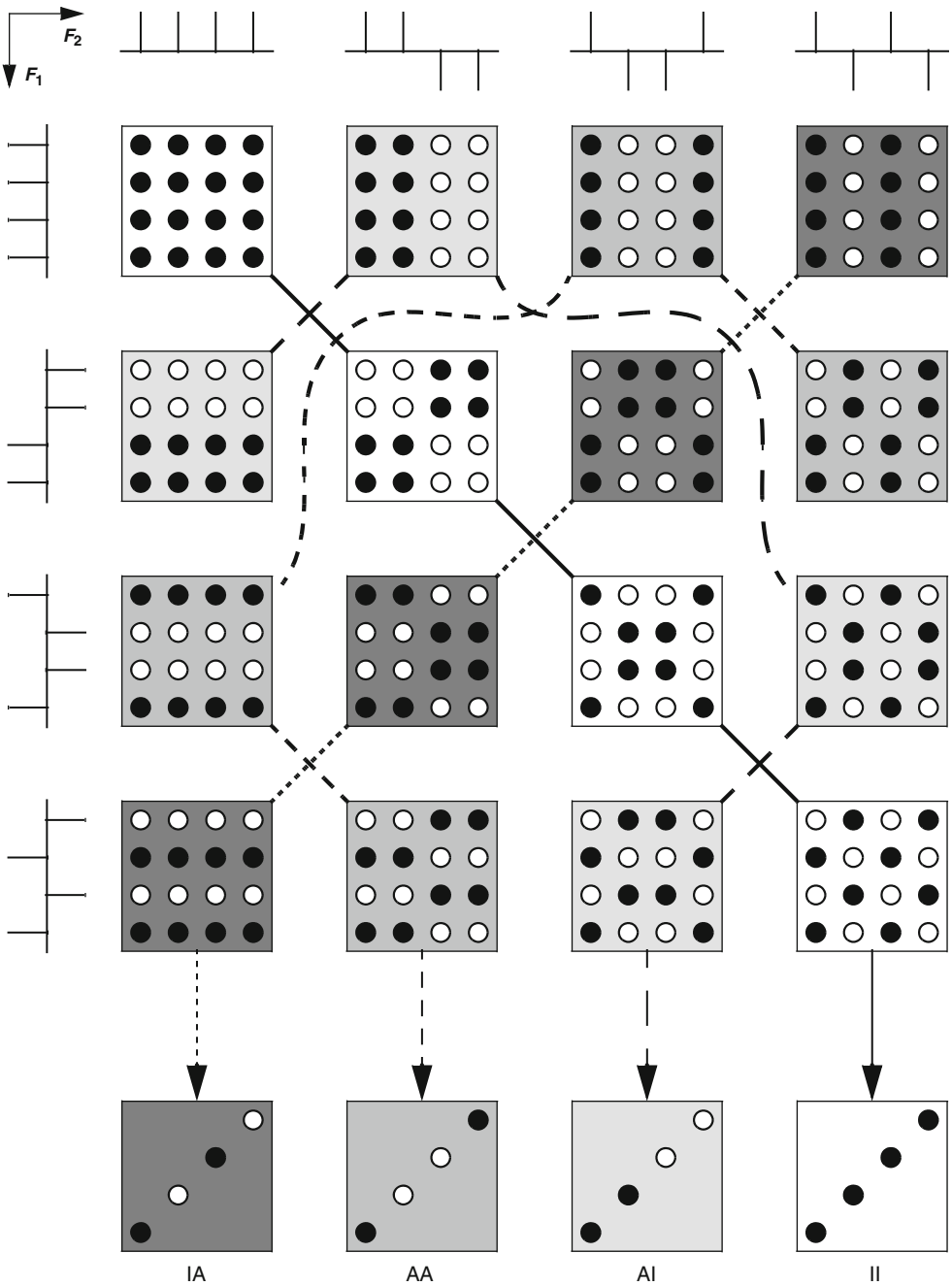

Fig. 4 Construction of E.COSY-type DIPAP constituents. Each of the four constituents denoted II, IA, AI, and AA, is composed of four out of 16 splitting patterns, such that positive and negative multiplet lines (*filled* and *open dots*) cancel to give the tilted E.COSY multiplet appearance. The reference IPAP experiment selects the patterns displayed on the diagonal and antidiagonal, generating exclusively II and IA constituents, while the DIPAP experiment utilizes all possible patterns in order to generate all four constituents. Component patterns within each group must carry equal weights, where unit weights are considered for the diagonal groups in both IPAP and DIPAP spectroscopy, while the additional multiplet groups collected in DIPAP only are attenuated due to *J*-dependent magnetization transfer according to $\sin({}^{1}J_{N'C_\alpha}\pi\delta)$ $\sin({}^{2}J_{C_\alpha N'}\pi\delta)$

RNase T1

Uniformly ^{13}C,^{15}N-doubly labeled recombinant 104-residue ribonuclease T1 from *Aspergillus oryzae*, obtained according to established protocols (Spitzner et al. 2001), was concentrated at 2 mM in aqueous solution (90% H_2O/10% D_2O) of pH 5.5 and measured at 303 K.

Xylanase

Recombinant ^{13}C,^{15}N-doubly labeled 207-residue family-11 xylanase from *Bacillus agaradhaerens* (Betz et al. 2002) was dissolved at 0.3 mM concentration in 10 mM sodium acetate buffer (pH 5.4) containing 5% D_2O, 0.03% NaN_3 and 50 μg/ml Pefabloc protease inhibitor. Measurements were carried out at 302 K.

Get2NTD

Get2NTD is the N-terminal cytosolic domain of one of several proteins composing the membrane receptor of the so-called Get complex responsible for the insertion of tail-anchored proteins into the ER membrane (Schuldiner et al. 2008). Get2NTD was overexpressed in T7 express

Table 1 Parameters used in [^{15}N,^{1}H]-TROSY-HN(CO-α/β-NCα-*J*)-DIPAP and reference-IPAP experiments

Sample	Common parameters			DIPAP				Reference IPAP	
	$t_{1,max}$(^{15}N) (ms)	$t_{2,max}$(^{1}H) (ms)	Total time (h)	Scheme	δ (ms)	Field (MHz)	Scans (×4)	Field (MHz)	Scans (×2)
Ubiquitin	215	81	10	A	48	500	8	500	16
RNase T1	222	85	10	A	48	500	8	500	16
Get2 NTD	210	80	17	B	48	600	16	600	32
Xylanase	152	60	63	A	45	950	24	900	48
				B	45	950	56	900	112
Proteorhodopsin	110	54	110	B	48	950	128	900	256

competent *E. coli* cells (Biolabs) at 17°C in the presence of 0.5 mM IPTG in M9 minimal medium supplemented with 1 g/l $^{15}NH_4Cl$ and 2 g/l $^{13}C_6$-glucose for the preparation of uniformly ^{13}C,^{15}N isotopically labeled protein. Following overnight induction, cells were harvested and stored at –80°C. Cells were resuspended in buffer A (50 mM Tris, 150 mM NaCl, 2% (vol/vol) glycerol, 2 mM β-Me, pH 7.5) and lysed by sonication in the presence of protease inhibitors. The lysate was first cleared by centrifugation at 17,000 rpm for 30 min at 4°C, then purified by affinity Ni–NTA agarose (QIAGEN), and bound Get2NTD eluted with buffer A supplemented with 250 mM imidazole. The protein was further purified by gel filtration (HiLoad 16/60 Superdex 75; GE Healthcare) in buffer containing 20 mM HEPES, 150 mM NaCl, 2% (vol/vol) glycerol, 1 mM DTT and 2 mM $MgCl_2$, pH 7.5). Overnight incubation with thrombin (1 U of protease/100 μg of protein) was followed by a second Ni–NTA agarose column to remove uncleaved product and the His_6 tag; the protease was separated using Benzamidine Sepharose 6B (GE Healthcare). Finally, Get2NTD was concentrated and dialyzed into the NMR buffer (50 mM HEPES, 50 mM NaCl, 1 mM DTT, pH 7.0). A 0.6-mM sample was used for measurements at a temperature of 283 K.

Proteorhodopsin

Green-absorbing proteorhodopsin (C90A, C158S double mutant) without signal peptide (residues 21–249) was cloned into a pIVEX2.3d vector and expressed in the continuous-exchange cell-free system based on an *E. coli* S30 extract (Schwarz et al. 2007). The detergent mode was used in the presence of 0.6 mM retinal (Sigma), containing 0.4% digitonin (Sigma) mixed with diC7PC (Avanti Polar Lipids) in a 4:1 molar ratio. For production of the NMR sample [u-^{13}C,^{15}N]-labeled amino acids (Cambridge Isotope Laboratories) were added directly to the reaction mixture. Subsequent Ni-affinity purification removed impurities from the extract and the detergent was exchanged into purely 0.1% diC7PC. Buffer exchange for NMR conditions (25 mM NaOAc pH 5, 2 mM DTT) was achieved on gravity flow PD-10 columns (GE Healthcare). The detergent added up during concentration to approximately 2% while the final protein concentration was 0.4 mM. NMR experiments were performed at 323 K.

NMR experiments

All measurements were carried out at least twice using Bruker Avance spectrometers operating at ^{1}H Larmor frequencies ranging from 500 to 950 MHz. A ^{1}H{^{13}C/^{15}N} triple-resonance probe with room-temperature three-axis gradient gear was used at 500 MHz while other spectrometers were equipped with cryogenic *z*-gradient triple-resonance probes (Table 1).

DIPAP and reference IPAP experiments applied to ubiquitin and RNase T1 employed the DIPAP pulse sequence illustrated in Fig. 3a. To Get2NTD and proteorhodopsin, the BEST-type pulse sequence of Fig. 3b was applied. Both schemes were applied to xylanase.

Pulse sequences employed in the present study for reference [^{15}N,^{1}H]-TROSY-HN(CO-α/β-NCA-*J*)-IPAP experiments derive from those in Fig. 3 by setting $\delta = \zeta = 33$ ms and by omitting the 180° $^{13}C^{\alpha}$ pulse from module **a** (module **b** not used in IPAP). Interleaved subspectra, inphase and antiphase with respect to $^{2}J_{C\alpha N'}$, were recorded by alternating between modules **c** and **d**.

Cosine-square and 60°-shifted sine-square apodization was applied to t_2 and t_1 data in all spectra prior to Fourier transformation.

Results and discussion

Collection and extraction of numerical parameters from NMR spectra for the purpose of molecular structure determination can be considered a process of two stages, each of which comes with specific limitations to accuracy. The first stage, data collection, includes both the NMR experimental design and the actual recording of spectral data. The second stage, data evaluation, picks up the processed data and seeks to extract the sought spin-system parameters. A certain experiment often requires a

certain evaluation method. Ideally, a balanced level of sophistication is sought for both stages.

Spin-state editing by Fourier transforms

In analogy to cosine and sine functions, inphase and antiphase doublets can be considered real and imaginary parts of some complex signal arising from bilinear rotation under J-coupling operator $\pi J_{IS} I_z S_z$. Two such rotations associated with C_i^α and C_{i-1}^α need to be considered in the present case. Data recorded for the four two-dimensional DIPAP spectrum constituents according to Fig. 3 were thus stored as a four-tier 3D stack. Combining all subspectra by applying Fourier transforms (FT), as shown in Fig. 5, locates individual multiplet lines whose frequency differences correspond to the sought J coupling constants. Not exactly associated with 'time' or 'frequency', this third dimension gives rise to a '*sequency*' domain, where individual spectra differ in the *number of nodes* in the multiplet structure.

In the simplest case, two input data combined yield the sum and difference output of the fundamental FT 'butterfly' unit (Fig. 5). The discrete Fourier transform (DFT) for the present case, $N = 4$, expressed in matrix form is (Bracewell 1986)

$$\begin{bmatrix} M_0 \\ M_1 \\ M_2 \\ M_3 \end{bmatrix} = \begin{bmatrix} 1 & 1 & 1 & 1 \\ 1 & w^1 & w^2 & w^3 \\ 1 & w^2 & w^4 & w^6 \\ 1 & w^3 & w^6 & w^9 \end{bmatrix} \times \begin{bmatrix} m_0 \\ m_1 \\ m_2 \\ m_3 \end{bmatrix}. \quad (6)$$

Assuming ^1J being larger than ^2J, the sequence constituting the real part of the 3D data array is $m_0 = \mathrm{II}$, $m_1 = \mathrm{AI}$, $m_2 = \mathrm{AA}$, and $m_3 = \mathrm{IA}$. While the all-positive II component cannot exhibit any node, multiplet lines in AI, AA, and IA alternate in sign, such as to generate along either frequency dimension 1, 2, and 3 nodes, respectively.

The sequency dimension now requires symmetric and antisymmetric multiplet patterns be stored in alternate memory locations in order to isolate, as the four DFT output matrices, the spin-state-edited multiplet lines denoted $M_0 = \alpha\alpha$, $M_1 = \alpha\beta$, $M_2 = \beta\beta$, and $M_3 = \beta\alpha$ associated with the two passive carbon spins C_i^α and C_{i-1}^α (Fig. 5).

The kernel in (6), $w = \exp(-i2\pi/N)$, as the N-th root of unity, represents a phase of $-i/N$ turns, or just $w = i$ here. Each of these complex factors, when applied to complex data, equates to a 90° phase rotation, effectively swapping real and imaginary parts including a sign change in one part, to yield

$$\begin{aligned} M_0 &= m_0 + m_1 + m_2 + m_3 \\ M_1 &= m_0 - m_2 + i(m_1 - m_3) \\ M_2 &= m_0 - m_1 + m_2 - m_3 \\ M_3 &= m_0 - m_2 - i(m_1 - m_3). \end{aligned} \quad (7)$$

It follows from (7) that the resulting constituents M_0 and M_2 represent pure real data, with zero imaginary parts, whereas M_1 and M_3 together form a complex-conjugate pair sharing identical real parts, their mixed-mode absorptive-dispersive lineshape apparently twisted in opposite directions. Periodic wrapping effects around the array boundary are expected as antisymmetric input patterns with implicit zero imaginary parts are effectively devoid of

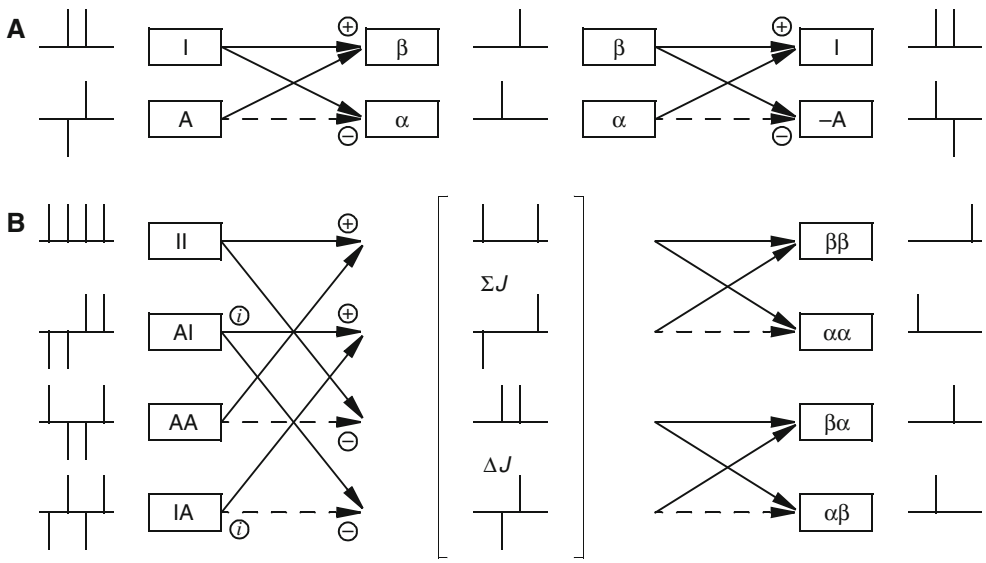

Fig. 5 **a** The principle of the fundamental 2-point FT 'butterfly' unit. Spin states are edited by forming data sums (*solid arrows*) and differences (*dashed arrows* indicate sign inversion). Two successive FTs yield the original IP and an inverted AP constituent. Four successive FTs reinstate the starting situation. **b** The 4-point FT applied to a doublet of doublets. Notice the pro-forma multiplet patterns enclosed in parentheses. It is not possible to capture any sensible intermediary patterns in the course of an FT operation. For algorithmic reasons, the output array sequence is scrambled but can be sorted by swapping data accordingly

directional information. Initially, as their intensity is spread out over both real and imaginary parts, the antisymmetric signals M_1 and M_3 exhibit lower S/N ratios than the symmetric signals M_0 and M_2. As no data must be discarded, co-addition of real and imaginary parts, separately so for each subspectrum, cancels all dispersive features, restores the total multiplet intensity, thereby equalizing S/N, and leaves M_1 and M_3 as pure real data (absorptive lines) also,

$$\begin{aligned} M_0 &= m_0 + m_1 + m_2 + m_3 \\ M_1 &= m_0 + m_1 - m_2 - m_3 \\ M_2 &= m_0 - m_1 + m_2 - m_3 \\ M_3 &= m_0 - m_1 - m_2 + m_3 \end{aligned} \tag{8}$$

These are the four subspectrum combinations depicted in Fig. 6. The operation is fully reverted by applying an inverse Fourier transform ($w = -i$ in (6)) with subsequent subtraction of imaginary from real parts.

S/N ratios appear higher in the spin-state edited spectra than in the respective IP/AP representation. Indeed, the four-fold (DIPAP) or twofold (IPAP) measurement effort was expended to 'record' the single lines, by combining subspectra. The correlated spectral information makes signal amplitudes stack up proportionately with the number of spectra added, whereas the uncorrelated noise rises slower. Conversely, transforming the four spin-state edited lines into IP/AP combinations, the signal amplitude decreases faster than the noise level, again, due to data correlation. As long as all constituents are being evaluated simultaneously, the lower S/N of the IP/AP representations does not pose any disadvantage in lineshape fitting procedures.

Spectrum analysis

All DIPAP and reference-IPAP spectra were processed and data analyzed as identically as possible, using Matlab-coded nonlinear least-squares fitting of 2D multiplet lineshapes (Schmidt 1997; Löhr et al. 2000). Multiplets of typically 32×64 data points were simultaneously extracted from the four data planes. Nitrogen and proton chemical shifts in ppm only served to locate signals in the F_1 and F_2 dimensions, respectively. The 2D Lorentzian lineshape model then provided parameters for positional fine-tuning and linewidths in both frequency dimensions, complemented by a number of generic E.COSY-type

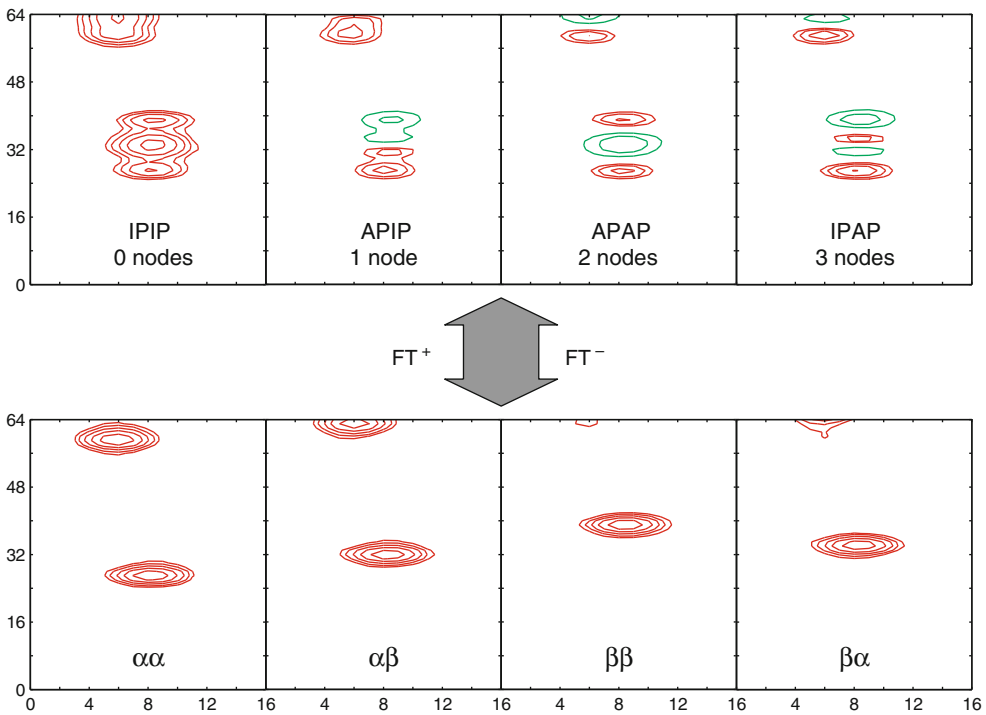

Fig. 6 Representations of DIPAP data for Ile90 in ribonuclease T1 showing (*top*) the 'nodes' or 'sequency' domain and (*bottom*) the 'spin-state' domain. *Red* and *green* contours denote positive and negative intensity, respectively. Spin-state edited spectra simultaneously emerge from complex Fourier transform of inphase and antiphase input constituents, provided these are sorted by an increasing number of multiplet nodes, and subsequent co-addition (FT^+) of real and imaginary parts. The process is fully reverted by inverse Fourier transform and subsequent co-addition of real and complex-conjugate imaginary parts, tantamount to subtracting imaginary from real parts (FT^-). *Unresolved lines* in the original spectra prevent direct determination of J coupling constants from multiplet splittings. *All lines* are readily resolved in the spin-state edited spectra and their positions accurately located for J coupling determination. *Axes* are labeled in arbitrary data points

J-splitting pairs as anticipated for the signal. For those two splitting-parameter pairs associated with C_i^{α} or C_{i-1}^{α}, time-domain signals were calculated using both cosine and sine modulation, such as to generate IP and AP doublets, respectively, following FT.

Additional parameters were supplied for modelling linewidth differentials between the pair of lines constituting each doublet, independently so for either splitting related to C_i^{α} or C_{i-1}^{α}. Including an overall amplitude-scaling parameter, a total 19 parameters were optimized for each multiplet (see Supplementary Material).

Apodization functions were modelled as used in spectrum processing, following the spectrometer vendor's handbook, and multiplied to the synthetic time-domain data. The first data point in either time dimension was halved to avoid baseline offsets. To account for first-order phase twists in F_2 due to evolution of the $J_{\mathrm{HNH}\alpha}$ coupling during the final period ($\tau' + \tau_{\mathrm{G}}$) in pulse sequence A, a fixed delay of 5.76 ms was inserted in the simulation time axis t_2 applied to homonuclear passive splittings.

Perturbation arising from overlapping multiplets was dealt with by simulating the affected patterns iteratively (Fig. 7).

The signals obtained for the 241-residue membrane protein proteorhodopsin in detergent micelles, a system of an apparent molecular size of 70-kDa, are compared in Fig. 8 for both the original [^{15}N,^{1}H]-TROSY-HN(CO-α/β-NC$^{\alpha}$-*J*)-IPAP and the new [^{15}N,^{1}H]-TROSY-HN(CO-α/β-NC$^{\alpha}_{\mathrm{i,i-1}}$-*J*)-DIPAP experiment. For this most challenging protein sample, 53 reasonably intense and isolated signals could be extracted from both DIPAP and reference IPAP spectra and subjected to multiplet fitting following the same protocol as for the other samples. While 29 of the DIPAP multiplets gave sensible results, only 15 of the IPAP multiplets converged without parameters straying unacceptably. In fact, optimized parameter values from the DIPAP fit were used to initiate the IPAP simulations as gently as possible. The results indicate that parameter optimization tends to be more robust with DIPAP than with IPAP data. This owes to the presence of the weak yet stabilising AA constituent in DIPAP, which is absent in IPAP. Its negative central lines help lock the multiplet position and reduce overall parameter variability. For this limited dataset, $^{1}J_{\mathrm{N'C}\alpha}$ and $^{2}J_{\mathrm{C}\alpha\mathrm{N'}}$ coupling constants, respectively, averaged 8.7 ± 2.7 and 6.6 ± 0.9 Hz in IPAP, and 9.7 ± 0.8 and 5.1 ± 1.7 Hz in DIPAP. The comparatively low average values reflect the fact that the majority of residues in proteorhodopsin are involved in α-helix secondary structure, giving smaller coupling constants naturally. The ^{15}N linewidth parameters were 7.4 ± 2.1 Hz in IPAP and 9.7 ± 3.8 Hz in DIPAP, the different means and standard deviations possibly reflecting the twice larger data sample size in DIPAP, and the predominance of narrower signals in the smaller IPAP dataset. The rms discrepancies between data pairs available from both IPAP and DIPAP, which included the four multiplets shown in Fig. 8, were 2.8 and 2.1 Hz for $^{1}J_{\mathrm{N'C}\alpha}$ and $^{2}J_{\mathrm{C}\alpha\mathrm{N'}}$ coupling constant, respectively. It is noted that a deuterated proteorhodopsin sample likely would have produced more accessible spectral parameters by way of narrower lines and a better S/N.

One advantage of the DIPAP method is the lower demand of spectrum area for the spin-state edited multiplet lines, allowing signals in congested spectral regions to be resolved. As demonstrated in Fig. 9 for partially unfolded Get2 N-terminal domain (156 aa, 16.4 kDa), not all of the ^{1}J doublets are resolved in the IPAP spectrum. This prevents both determination of the coupling pair $^{1}J_{\mathrm{N'}(i)\mathrm{C}\alpha(i)}/^{2}J_{\mathrm{HN}(i)\mathrm{C}\alpha(i)}$ (along F_1/F_2) and accurate measurement of displacements between α and β states of C_{i-1}^{α} and the associated coupling pair $^{2}J_{\mathrm{C}\alpha(i-1)\mathrm{N}(i)'}/^{3}J_{\mathrm{C}\alpha(i-1)\mathrm{HN}(i)}$. By contrast, the singlets in DIPAP spectra are readily resolved and less prone to overlap.

Leakage pathways and *J*-dependent amplitudes

As stated in the context of (1), magnetization transfer pathways exist that cannot be eliminated by pulse-phase cycling in pulse-sequence module **a** or **b** and, therefore, complement the AA und AI subspectra with spurious II and IA components, respectively. Define, for the purpose of compactness, the amplitude factors

$$\begin{aligned} ss &= \sin\left(^{1}J_{\mathrm{N'C}\alpha}\pi\delta\right)\sin\left(^{2}J_{\mathrm{C}\alpha\mathrm{N'}}\pi\delta\right) \\ cc &= \cos\left(^{1}J_{\mathrm{N'C}\alpha}\pi\delta\right)\cos\left(^{2}J_{\mathrm{C}\alpha\mathrm{N'}}\pi\delta\right), \end{aligned} \tag{9}$$

and the composite couplings

$$\begin{aligned} \Sigma J &= (^{1}J_{\mathrm{N'C}\alpha} + ^{2}J_{\mathrm{C}\alpha\mathrm{N'}}) \\ \Delta J &= (^{1}J_{\mathrm{N'C}\alpha} - ^{2}J_{\mathrm{C}\alpha\mathrm{N'}}), \end{aligned} \tag{10}$$

then, the respective multiplets (2) develop according to

$$\begin{aligned} M_{\mathrm{II}} &= \mathrm{II} \times 1 \\ M_{\mathrm{IA}} &= \mathrm{IA} \times 1 \\ M_{\mathrm{AI}} &= \mathrm{AI} \times ss - \mathrm{IA} \times cc \\ M_{\mathrm{AA}} &= \mathrm{AA} \times ss - \mathrm{II} \times cc \end{aligned} \tag{11}$$

The *cc*-modulated leakage signals are minimal if the magnetization-transfer period δ equals either $(2\ ^{1}J_{\mathrm{N'C}\alpha})^{-1}$ or $(2\ ^{2}J_{\mathrm{C}\alpha\mathrm{N'}})^{-1}$. With average ^{1}J and ^{2}J values of 10.7 and 7.7 Hz, respectively, the *cc* term vanishes for δ periods around 46–48 and 62–68 ms. At the *ss*-transfer maximum in the intervening range around 54–55 ms, *cc* takes on slightly positive values (Fig. 10).

The condition $ss = cc$ is met if δ equals half the optimal period, i.e., at around 30 ms or, again, at around

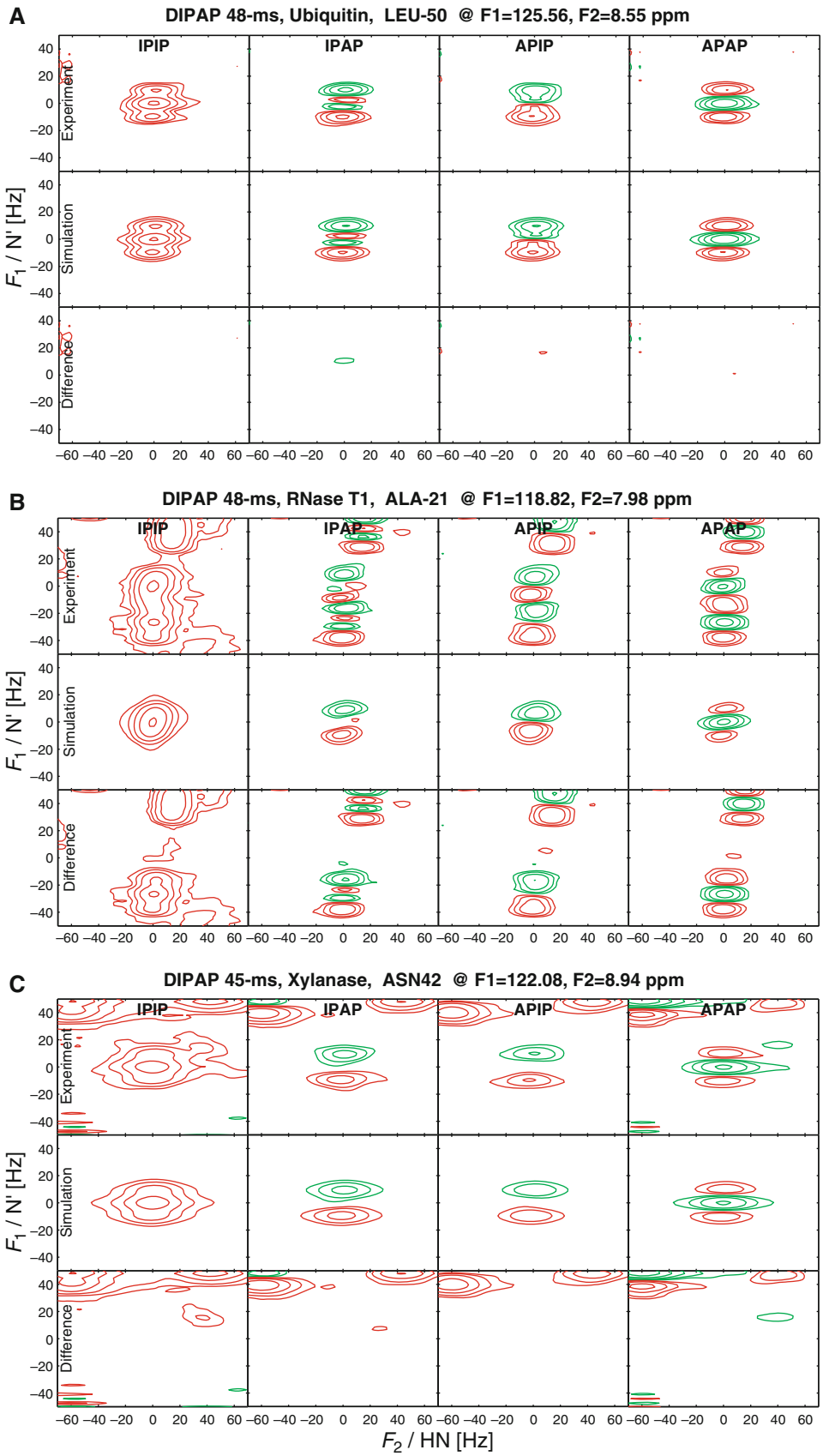

Fig. 7 Representative $^{15}N,^{1}H^{N}$-TROSY-HN(CO-α/β-$NC^{\alpha}_{i,i-1}$-*J*)-DIPAP multiplet evaluations by simultaneous 2D lineshape fitting of its four constituents. **a** The Leu50 multiplet in the 500-MHz 48-ms DIPAP spectrum of ubiquitin exhibits typical line splittings in the vertical dimension of 8.64 and 10.80 Hz for $^{2}J_{C\alpha N'}$ and $^{1}J_{N'C\alpha}$, respectively, with associated $^{3}J_{C\alpha HN}$ and $^{2}J_{HNC\alpha}$ coupling constants of 1.74 and 0.78 Hz in the horizontal direction. **b** The 500-MHz 48-ms DIPAP spectrum of RNase T1 shows, partly overlapped by the Ser54 multiplet, the Ala21 multiplet with a pattern typical of an α-helical residue, where coupling constants $^{2}J_{N'C\alpha}$, $^{1}J_{N'C\alpha}$, $^{2}J_{HNC\alpha}$, and $^{3}J_{C\alpha HN}$ are 5.97, 9.57, 2.56, and 0.12 Hz, respectively. **c** The Asn42 multiplet in the 950-MHz 45-ms BEST-DIPAP spectrum of xylanase shows $^{2}J_{N'C\alpha}$ at 9.50 Hz exceeding $^{1}J_{N'C\alpha}$ at 9.34 Hz. The associated couplings $^{3}J_{C\alpha HN}$ and $^{2}J_{HNC\alpha}$ are 0.39 and 2.14 Hz, respectively

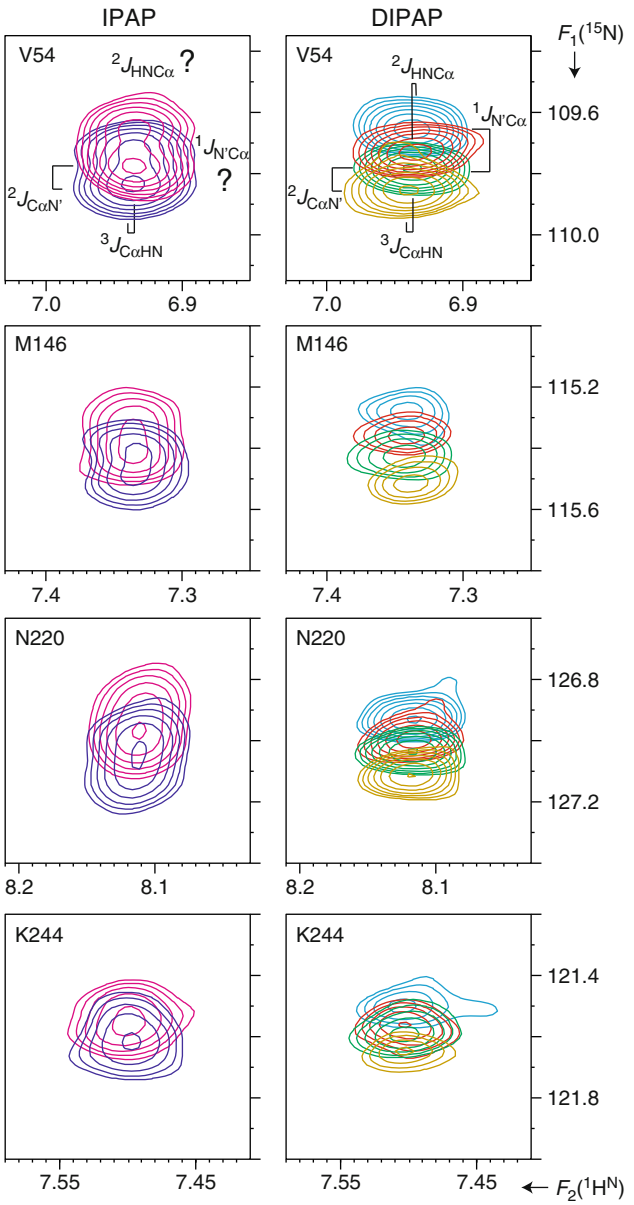

Fig. 8 Breakdown of individual multiplet components selected from (*left*) HN(CO-α/β-NC$^{\alpha}$-*J*)-IPAP and (*right*) HN(CO-α/β-NC$^{\alpha}_{i,i-1}$-*J*)-DIPAP spectra of proteorhodopsin. Only DIPAP allows the individual multiplet lines to be resolved, which are encoded in different colour. Each multiplet of residue *i* exhibits two pairs of vertical and horizontal line splittings, due to one IPAP pattern from $^2J_{C\alpha(i-1)N'(i)}$ and $^3J_{C\alpha(i-1)HN(i)}$, and another from $^1J_{N'(i)C\alpha(i)}$ and $^2J_{HN(i)C\alpha(i)}$

80 ms. Notice, however, that only partial multiplet cancellation can occur as AI and IA as well as II and AA are pairwise different patterns.

Transfer function optimization

Transfer amplitudes due to the second filter period, ε, equally present in both DIPAP and reference-IPAP experiments, is to match the fairly uniform $^1J_{C\alpha C'}$ coupling of 52.6 ± 0.9 Hz in all amino acids (Schmidt et al. 2009). Taking overall relaxation into account, our choice falls on the shorter end, $\varepsilon = 9.2$ ms, producing only negligible signal attenuation of less than 1% between both IP(^1J) and AP(^1J) pathways, and it is safe to consider $\cos(^1J_{C\alpha C'}\pi\varepsilon) = 0$ and $\sin(^1J_{C\alpha C'}\pi\varepsilon) = 1$ in the following.

However, the intensities of constituent multiplets AA and AI, present only in the DIPAP experiment, depend on the critical pulse-sequence duration δ which is to match typical values of $^2J_{C\alpha N'}$ and $^1J_{N'C\alpha}$ in the peptide spin topology.

As both N,C$^{\alpha}$ couplings are fully refocussed, the delay δ could be as short as approximately 33 ms, so as to allow full evolution of the $^1J_{N'C'}$ coupling. However, this would benefit the II and IA constituents only.

Consider the expansions

$$\begin{aligned} ss &= (1/2)[\cos(\pi\delta\Delta J) - \cos(\pi\delta\Sigma J)] \\ cc &= (1/2)[\cos(\pi\delta\Delta J) + \cos(\pi\delta\Sigma J)] \end{aligned} \tag{12}$$

To optimize the transfer function,

$$M(\delta) = ss - cc = -\cos(\pi\delta\Sigma J), \tag{13}$$

its derivative with respect to δ,

$$dM/d\delta = \pi\Sigma J \sin(\pi\delta\Sigma J), \tag{14}$$

would need to become zero. As the sum of both (negative) coupling constants is clearly not zero, the sought condition is $\delta_{opt} = (\Sigma J)^{-1}$. Perfect transfer would further require both—mathematically fully interchangeable—couplings be of identical magnitude, regardless of sign. As values of ^1J and ^2J clearly differ in real proteins, the total transfer efficiency, i.e., the summed *ss* and *cc* terms, can only be less than unity, because $\sin(a)\ \sin(b) + \cos(a)\ \cos(b) = \cos(a - b)$, implying that the larger the coupling difference the more attenuated the multiplet intensity. Sums and differences between ^1J and ^2J typically amount to 19 and 3 Hz, respectively, so the optimal value of δ would be just *above* 50 ms (Fig. 10).

Magnitudes of $^2J_{C\alpha N'}$ and $^1J_{N'C\alpha}$ in α-helix secondary structure are 6.1 and 9.5 Hz, respectively, resulting in a longer transfer period δ of around 64 ms and an attenuation of 12% on the *ss* term. Couplings of 8.5 and 11.0 Hz in β-sheet conformation command a shorter period of 51 ms (4% attenuation). On average, $^2J_{C\alpha N'}$ and $^1J_{N'C\alpha}$ of 7.7 and 10.7 Hz, respectively, indicate $\delta = 54$ ms (6% attenuation).

The additional *cc*-modulated leakage term is negligible if δ values meet the zero condition. Therefore, a δ value set at just *under* 50 ms helps minimize the *cc* term, at the expense of only a few percent in lost transfer efficiency.

For other, possibly deliberately misadjusted values of δ, when the *cc* term contributes either negative or positive intensity, inclusion of this term in multiplet evaluations is

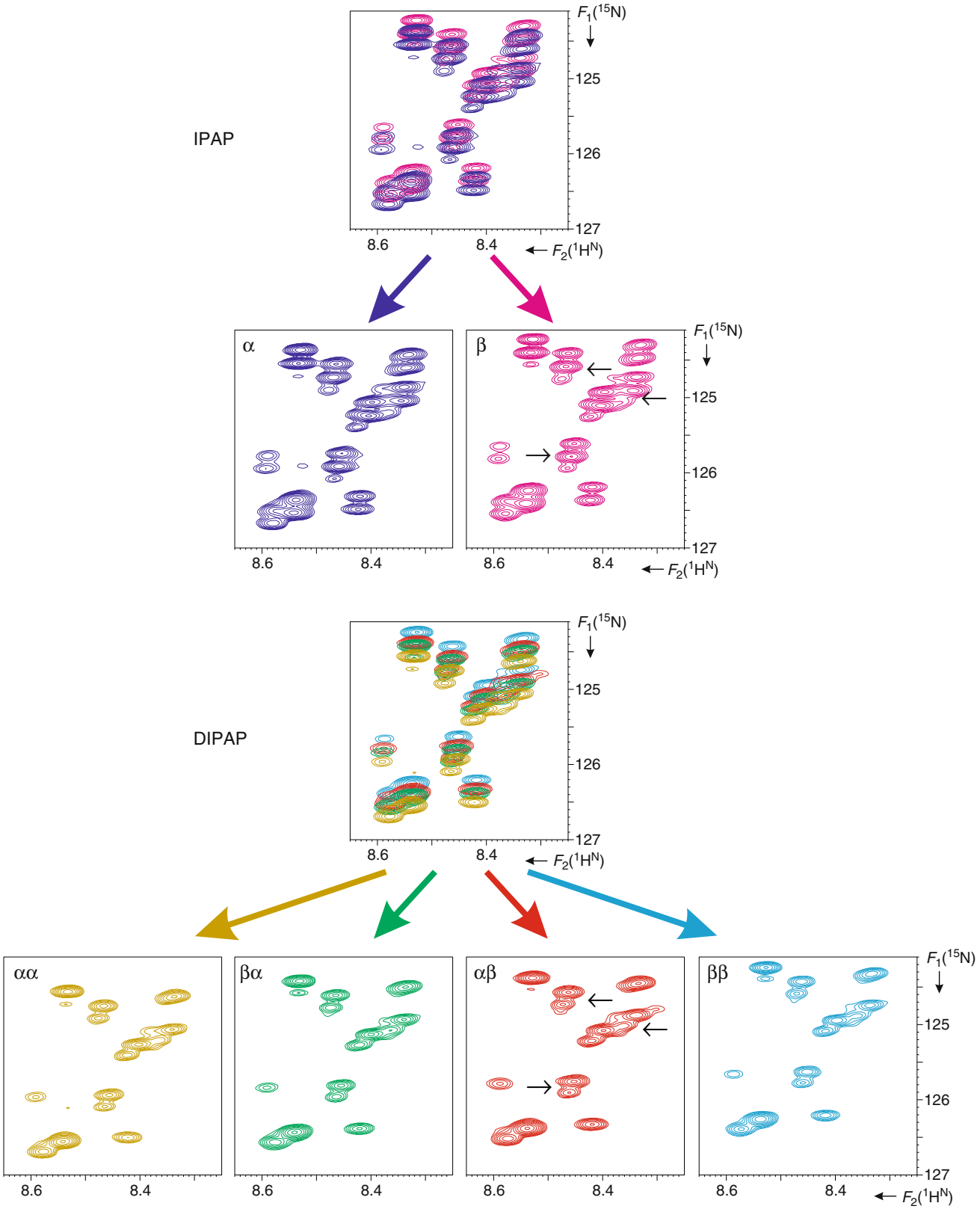

Fig. 9 Excerpts from (*top*) HN(CO-α/β-NC$^{\alpha}$-*J*)-IPAP and (*bottom*) HN(CO-α/β-NC$^{\alpha}_{i,i-1}$-*J*)-DIPAP spectra of partially unfolded Get2 protein, illustrating the reduced signal overlap in the DIPAP approach. Colour coded spin-state-selected subspectra are shown superimposed as well as separated. *Arrows* in *panels* β and $\alpha\beta$ point at groups of peaks that cannot be resolved in IPAP spectra

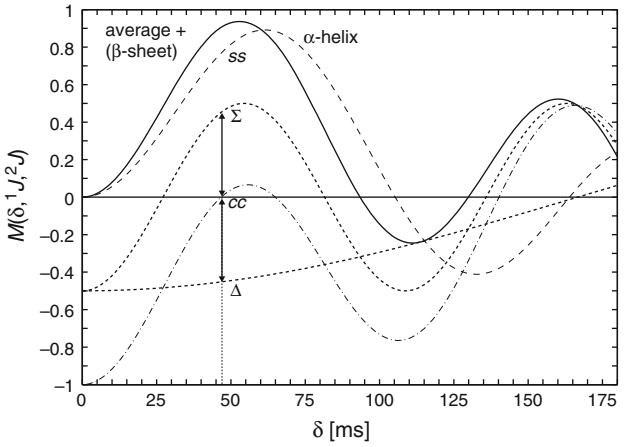

Fig. 10 Magnetization transfer for AA/AI constituents in TROSY-HN(CO-α/β-$NC^{\alpha}_{i,i-1}$-J)-DIPAP. The *solid curve* labeled 'average' is the principal transfer function, using literature values of 7.7 and 10.7 Hz for $^{2}J_{C\alpha N'}$ and $^{1}J_{N'C\alpha}$ couplings, respectively. The *dashed curve* labeled 'α-helix' uses 6.1 and 9.5 Hz. After the critical period δ of 50-55 ms, AA and AI multiplet intensities have risen, according to $ss = \sin(^{1}J\pi\delta)\ \sin(^{2}J\pi\delta)$, to approximately 93% of the II and IA multiplet intensities not subject to this transfer function. Residual II and IA multiplets of intensity $cc = -\cos(^{1}J\pi\delta)\ \cos(^{2}J\pi\delta)$ overlay the AA and AI multiplets, respectively, the effect being minimal near 45 and 65 ms (*dash-dotted line*). *Dotted curves* represent modulations by sum and difference couplings, $\Sigma = \cos(\pi\delta(^{2}J + {}^{1}J))$ and $\Delta = \cos(\pi\delta(^{2}J - {}^{1}J))$, i.e., outer and inner multiplet line intensities (also see Fig. 11, best appreciated in the AA multiplet). While the (negative) inner lines diminish only gradually with increasing δ, the outer lines undergo faster oscillation, vanishing at around 30 and 80 ms for δ. An appropriate choice of δ just under 50 ms minimises the spurious cos × cos terms and, at the same time ensures inner and outer lines are of comparable intensity (*arrows*). Relaxation effects are disregarded in this simulation but would tend to shift all extrema toward slightly shorter values of δ

indispensible. The effect of different transfer periods was tested by recording on RNase T1 a series of spectra with δ varying between 26 and 116 ms in steps of 6 ms (Fig. 11). Modified pulse programs were used for recording spectra with the short δ periods of 26 and 32 ms, so as to maintain full evolution of the $^{1}J_{C'N'}$ coupling over the constant duration $\zeta = 33$ ms.

Recognising the pairs of outer and inner lines of the double-doublets as sum and difference splittings, respectively, (10) and (12) rationalise the oscillatory behaviour of the AA and AI multiplet patterns. Best observed in the AA constituent, the outer lines pass through zero, i.e., *ss* and *cc* transfer terms cancel, at a short δ interval in the region of 25–30 ms. Obviously, the exact time at which the lines disappear depends on the actual coupling constants in the given residue. Similarly, another zero occurs after around 70 ms.

For the majority of residues, the AA constituents turn completely negative for δ periods above 80 ms, as the inner line pair is decaying only slowly, and the outer lines have passed three quarters of their cycle.

Fig. 11 Dependence of DIPAP constituents on the choice of experiment parameter δ. Intensities of II and IA constituents diminish due to relaxation loss only, whereas AI and AA constituents depend on the transfer function modulated by the sum (ΣJ) and difference (ΔJ) of both $^{1}J_{N'C\alpha}$ and $^{2}J_{C\alpha N'}$ couplings. (*Panels on the left*) Arg77 in RNase T1 represents the typical situation where couplings differ by approximately 3 Hz, best recognized by the slowly oscillating (negative) inner lines in the AA multiplet that subsequently invert at $\delta = 1/(2\Delta J) \approx 190$ ms. (*Panels on the right*) The much larger difference coupling in Val52 inverts the inner lines already after $\delta = 80$ ms. In both AI and AA multiplets, the large sum coupling of typically 18-20 Hz nulls the faster oscillating outer lines at $\delta = 1/(2\Sigma J) \approx 26$ ms and $\delta = 3/(2\Sigma J) \approx 80$ ms. In the majority of cases, an optimal value of δ near 48 ms produces the largest amplitudes and, at the same time, suppresses the spurious II and IA overlays on AA and AI, respectively

At approximately 110 ms for δ, as magnetization transfer related to the sum of both J couplings reaches another maximum, a splitting pattern is anticipated in which the outer lines have largely recovered to an intensity exceeding that of the inner lines which, related to the difference coupling, have decreased to about half their initial intensity.

The II and IA intensities are unaffected by oscillations and subject to relaxation only, as seen by gradually decreasing amplitudes overall.

Given the difference coupling is 3 Hz on average, the inner lines diminish slowly and would normally change sign only after 160 ms. The rare case of Gly88 in RNase T1, part of a β-bulge secondary-structure motif, exhibits the widest gap between the large ^{1}J coupling of 13.6 Hz and the small ^{2}J coupling of 6.5 Hz. An effective difference coupling of 7.1 Hz and correspondingly fast intensity undulation turn the inner lines positive after around 70 ms already.

Relaxation losses left aside, overview plots resulting from superimposing the four spin-state edited DIPAP spectra look similar for all values of δ. They essentially show the II portion (leftmost panels in Fig. 11), corresponding in the FT decomposition of (8) to data point M_0 that contributes the spectrum net intensity. The effects observed in the other patterns are of truly differential nature, as only relative amplitudes change between the various pairs of subspectra and between the pair of lines within each doublet.

Incomplete spin-state editing due to attenuated *ss*-magnetization transfer can be improved by applying weights either simply numerically or even experimentally, e.g., by accumulating different relative numbers of transients for IP(^{1}J) and AP(^{1}J) portions (see Supplementary Material).

Differential-relaxation effects

Amplitude and lineshape differences between the DIPAP (and reference-IPAP) multiplet constituents are primarily

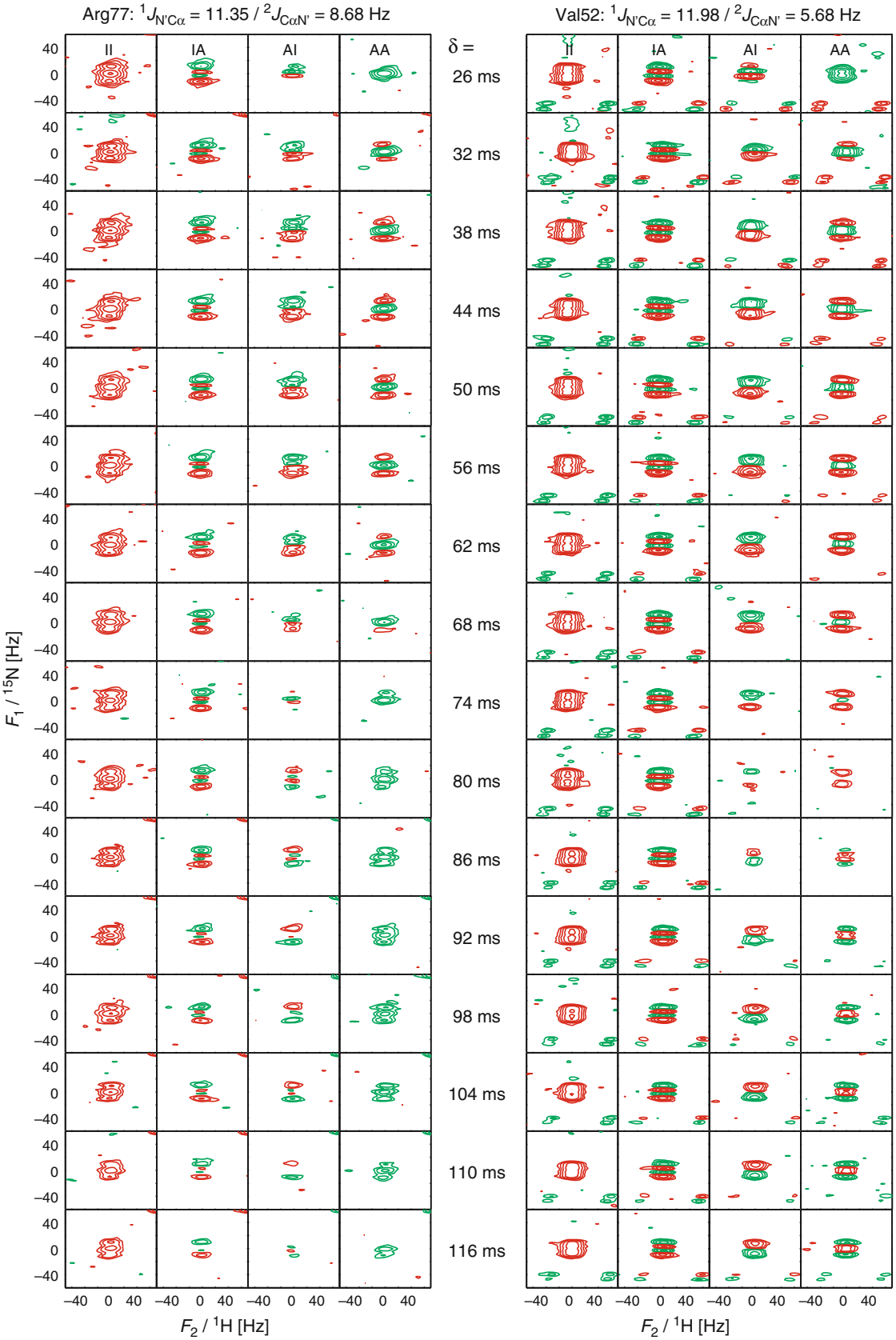
Arg77: $^1J_{N'C\alpha}$ = 11.35 / $^2J_{C\alpha N'}$ = 8.68 Hz
Val52: $^1J_{N'C\alpha}$ = 11.98 / $^2J_{C\alpha N'}$ = 5.68 Hz
II
IA
AI
AA
δ =
26 ms
32 ms
38 ms
44 ms
50 ms
56 ms
62 ms
68 ms
74 ms
80 ms
86 ms
92 ms
98 ms
104 ms
110 ms
116 ms
40
0
−40
F_1 / ^{15}N [Hz]
F_2 / ^{1}H [Hz]

attributed to coherent phenomena fully described by the J coupling situation and the magnetization transfer function. Dissipative effects, such as differential relaxation, may play a secondary role but cannot be excluded. Two types need to be considered: (1) lineshape differences within the same multiplet, e.g., inner versus outer lines of a doublet-of-doublets, and (2) amplitude differences between separate multiplets, e.g., M_{II} versus M_{AA}. While the first phenomenon is associated with the evolution and acquisition periods constituting the time domain variables of the spectrum, t_1 and t_2, respectively, the second effect takes place mainly during the constant magnetization-transfer period δ.

Dipole–dipole auto-correlation

E.COSY spectroscopy requires the states of the passively coupled C^{α} spins be preserved during and between evolution and acquisition periods, t_1 and t_2, respectively. However, in a protein, dipolar interaction with the attached $^{1}H^{\alpha}$ spins relaxes the C^{α} spins most efficiently and, thus, perturbs their supposedly preserved z-components. Consequently, differential relaxation between IP and AP doublet components occurs (Vuister and Bax 1993; Kuboniwa et al. 1994).

The Hamiltonian governing dipolar coupling interaction between spins i and j, here $^{1}H^{\alpha}$ and $^{13}C^{\alpha}$, respectively, scales with the interaction constant (Kumar et al. 2000)

$$\xi_{\mathrm{ij}} = (\gamma_i\gamma_j/r_{\mathrm{ij}}^3)\,(h/2\pi)(\mu_0/4\pi), \tag{15}$$

which equates to $\xi_{\mathrm{ij}}/\pi = 43.3$ kHz, given the gyromagnetic ratios, γ, for ^{1}H and ^{13}C, Planck's constant, h, the vacuum permeability, μ_0, and an effective C^{α}–H^{α} bond length of $r_{ij} = 111.7$ pm (Ottiger and Bax 1998). The rate contribution to C^{α}-longitudinal relaxation (in rad s^{-1}) is then approximated by

$$\Gamma_{\mathrm{ij},ij} = (3/10)\xi_{\mathrm{ij}}^2(2\tau_{\mathrm{c}})/(1+\omega^2\tau_{\mathrm{c}}^2). \tag{16}$$

Inserting isotropic molecular reorientational correlation times of 4.1 ns rad^{-1} for ubiquitin (Schneider et al. 1992), and of 5.3 ns rad^{-1} for RNase T1 (Fushman et al. 1994), (16) yields for 11.7-T field, or 125-MHz ^{13}C Larmor frequency, C^{α}-longitudinal relaxation rates $\Gamma_{\mathrm{H\alpha C\alpha,H\alpha C\alpha}}/\pi$ of 1.26 and 1.01 s^{-1}, respectively. These compare with experimental $T_1(C^{\alpha})$ relaxation times of 580 ms for ubiquitin at 125 MHz (Wand et al. 1996) and of 650 ms for RNase at 150 MHz (Engelke and Rüterjans 1995), indicating that C^{α}-passive-spin flips may be caused not only by dipolar auto-relaxation alone.

The influence of auto-correlated relaxation is expected to decrease as T_1 relaxation times typically increase with increasing molecular reorientational correlation time. Depending on temperature, T, and the number of amino-acid residues in the protein, N, the empirical formula (Daragan and Mayo 1997)

$$\tau_{\mathrm{c}} = \left(9.18\times10^4/T\right)\exp(2416/T)N^{0.93} \tag{17}$$

estimates τ_{c} for xylanase at 13 ns rad^{-1}. For proteorhodopsin in micelles, a value of 23 ns rad^{-1} was obtained experimentally using TRACT (Lee et al. 2006). The resulting long C^{α}-longitudinal relaxation times would leave nitrogen transverse relaxation as the predominant effect on both IP and AP signal line-widths in the F_1 dimension, which would depend approximately linearly on τ_{c}, and equally so for all four DIPAP constituents (Boisbouvier and Bax 2002).

Dipole–dipole cross-correlation

Temporal and spatial correlation between interaction vectors N'–$C^{\alpha(i)}$ and N'–$C^{\alpha(i-1)}$ causes dipole–dipole cross-correlated relaxation affecting the spin modes N_x and $N_xC_z^{\alpha(i)}C_z^{\alpha(i-1)}$ (patterns II and AA) and leads to linewidth differences between inner and outer lines of the doublet-of-doublets (Kumar et al. 2000). As gyromagnetic ratios of all involved nuclei are small, this contribution is rather insignificant. Indeed, iterative lineshape fitting showed near-zero ^{15}N differential linewidths in the F_1 dimension.

More likely, dipole–dipole cross-correlated relaxation between H^{N}–$C^{\alpha(i)}$ and H^{N}–$C^{\alpha(i-1)}$ vectors would affect H_x^{N} and $H_x^{N}C_z^{\alpha(i)}C_z^{\alpha(i-1)}$ spin modes and, thus, the multiplet fine structure along the F_2 dimension. Least-squares fitting results indicated, however, that cross-relaxation rates are on the order of 0.1 Hz only.

Owing to the involvement of shorter pair distances and numerous high-γ nuclei, dipole–dipole cross-correlated relaxation between vectors H^{N}–$C^{\alpha(i)}$ and H^{N}–$H^{\alpha(i)}$, giving rise to $^{1}H^{N}$ differential linewidth, seems most likely to distort the $^{2}J_{\mathrm{HNC\alpha}}$ splittings in particular (Yao et al. 2009; Guo et al. 2010).

In an experimental approach to exploring the effect of $^{1}H^{\alpha}$ relaxation on the coupling constants, a deuterated sample of ubiquitin was measured and the result compared with that from the non-deuterated sample. $^{2}J_{\mathrm{HNC\alpha}}$ coupling constants obtained from the fully protonated sample are on average by 0.4 Hz smaller than in the deuterated sample. Discrepancies in the other coupling types are on the order of 0.1 Hz for $^{3}J_{\mathrm{C\alpha HN}}$, and just above 0.2 Hz for either of the large splittings $^{1}J_{\mathrm{N'C\alpha}}$ and $^{2}J_{\mathrm{C\alpha N'}}$ (Fig. 12). And yet, including $^{1}H^{N}$–$^{13}C^{\alpha}$, $^{1}H^{N}$–$^{1}H^{\alpha}$ dipole–dipole cross-correlation rates in the multiplet simulations increased the average $^{2}J_{\mathrm{HNC\alpha}}$ coupling constant only marginally by 0.12 Hz, while effects on other couplings were negligible.

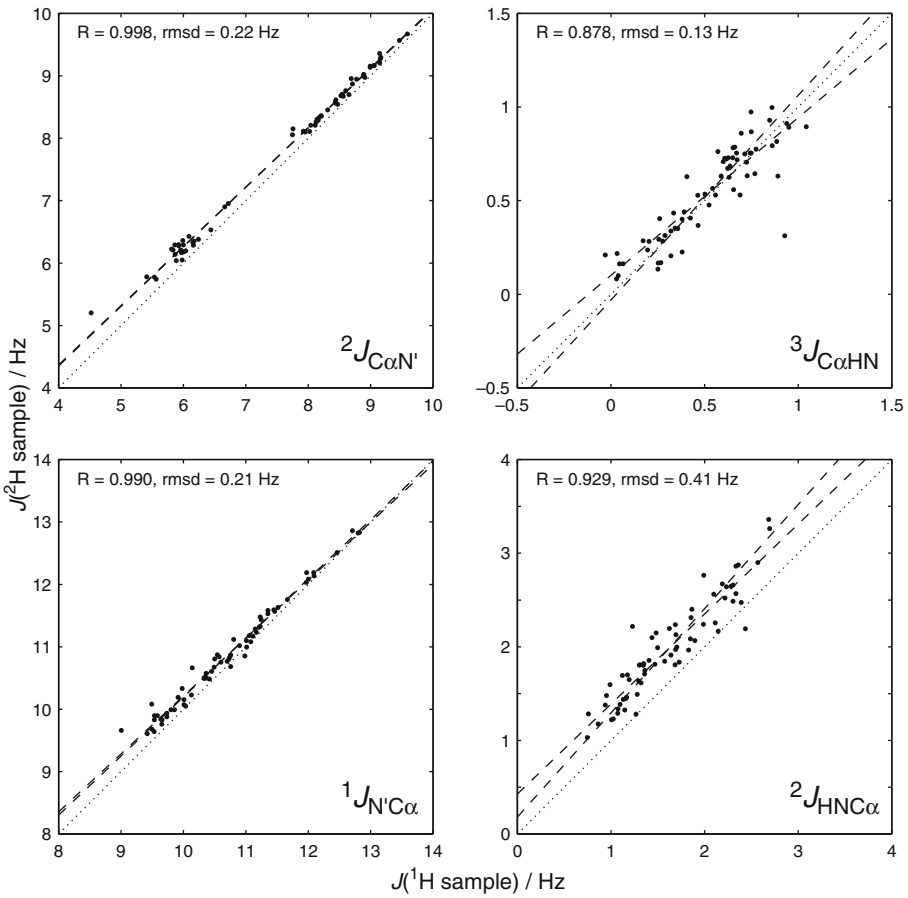

Fig. 12 Relaxation effects on coupling constants extracted from [^{15}N,^{1}H]-TROSY-HN(CO-α/β-NC$^{\alpha}_{i,i-1}$-J)-DIPAP multiplets. Fitted values of J from uniformly ^{13}C,^{15}N,70%-^{2}H-labeled (deuterated) ubiquitin against values from uniformly ^{13}C,^{15}N-labeled (protonated) ubiquitin demonstrate the effect of differing ^{13}C$^{\alpha}$-longitudinal relaxation rates in the absence and presence of the ^{1}H$^{\alpha}$ spin. On average, all J values are larger for the deuterated sample (also see Supplementary Material). *Dashed lines* represent linear regressions. The outlier in panel $^3J_{C\alpha HN}$ is Gly10 with coupling constants differing by 0.6 Hz between samples, most likely due to variation in relaxation rates affected by conformational dynamics (Schneider et al. 1992; Wand et al. 1996). Gly10 follows a type-I β turn and exhibits a positive ϕ torsion angle

An estimate of the dipole–dipole cross-correlated relaxation rate is given by

$$\Gamma_{ij,kl} = (2\tau_c/5)P_2(\cos\theta)\xi_{ij}\xi_{kl}. \quad (18)$$

Depending chiefly on spectral density at $\omega = 0$, the rate increases field-independently and linearly with τ_c. Dipolar interaction constants from (15) are 6.2 and 19.5 kHz, respectively, for the fixed distance $r_{HN-C\alpha} = 214$ pm and for the shortest possible distance $r_{HN-H\alpha} = 230$ pm. In this worst-case scenario assuming a rigid molecular conformation, differential broadening between outer and inner line pair would be $\Gamma_{HNC\alpha,HNH\alpha}/\pi = 0.6$ Hz in ubiquitin.

$P_2(x)$, the second-rank Legendre polynomial, is near unity as the short H$^{\alpha}$–C$^{\alpha}$ bond distance keeps the angle subtended by both vectors H^N–C$^{\alpha}$ and H^N–H$^{\alpha}$ within $\theta_{max} = 28°$, thereby limiting the value range of P_2 to 1.00 … 0.86. When the polypeptide torsion $\phi \approx +60°$, the *cis*-periplanar arrangement orients all three vectors in a plane, and C$^{\alpha}$–H$^{\alpha}$ closest to the affected spin H^N. This gives the largest possible rate contribution mentioned above, where the $^2J_{HNC\alpha}$ coupling, taking elevated values above 2 Hz for this geometry (Schmidt et al. 2010), would be the one most affected by cross-correlation effects. Positive ϕ torsion angles, however, are rare in polypeptide structure. For any other backbone conformation, smaller cross-correlated relaxation rates are anticipated, consistent with simulation results.

CSA-dipole cross-correlation

Unless ^{13}C$^{\alpha}$ spin states are inverted during the semi-constant-time evolution period t_1, cross-correlated relaxation effects between ^{15}N-chemical-shift anisotropy and ^{15}N,^{13}C$^{\alpha}$-dipolar interaction may give rise to differential linewidths within each doublet in F_1. This would concern both DIPAP and reference-IPAP spectra equally. However, the low gyromagnetic ratios of the nuclei involved should render this influence negligible. A similar yet non-negligible effect applies in F_2, originating from anisotropy of the ^{1}H^N chemical shift on the ^{1}H^N,^{13}C$^{\alpha}$ doublets (Yao et al. 2010b) which was found to be on the order of 0.1–0.2 Hz (Supplementary Material). Finally, present in both F_1 and F_2 dimensions, the interference between the ^{1}H^N,^{15}N$'$ dipole with ^{15}N$'$ and ^{1}H^N chemical-shift anisotropies has, in fact, been exploited for selecting the TROSY line when recording the spectra (Pervushin et al. 1997).

DIPAP and reference IPAP spectra were recorded at slightly different field strengths for both xylanase and proteorhodopsin (Table 1). Even though scalar coupling constants are to a first approximation field independent, comparison of results from both spectra may be affected by potential differences in the field-dependent TROSY effect exploited to accomplish line narrowing through advantageous cancellation of ^{1}H,^{15}N dipolar and ^{15}N CSA interaction (Pervushin et al. 1997; Pervushin 2000), as varying linewidths or resolution may translate into variation in the line splitting or coupling parameters determined. However, no significant effects are anticipated for reasons that follow. On average, the most narrow ^{1}H linewidth is accomplished by TROSY applied to isotropically tumbling samples at around 924 MHz (Fushman and Cowburn 2001), implying that both fields employed would result in similar effects along the F_2 multiplet dimension. However, to maximize the TROSY effect on the ^{15}N linewidth, the optimal field strength identified—in terms of proton Larmor frequency—is about 800 MHz (Yao et al. 2010a, b). Regarding the ^{15}N dimension in which both $^{1}J_{\mathrm{N'C\alpha}}$ and $^{2}J_{\mathrm{C\alpha N'}}$ coupling constants are measured, if any, this fact would give our reference IPAP spectra recorded at the lower of both fields a slight linewidth and sensitivity advantage over the corresponding DIPAP spectra. It was furthermore found that conformation-dependent local variation from residue to residue both in CSA tensor geometry and in the relative orientation between dipolar and CSA tensors influences the TROSY effect considerably more than the comparatively flat B_0 field dependence, especially in the range of 900–950 MHz (Fushman and Cowburn 2001; Yao et al. 2010a, b). Finally, for non-deuterated proteins the field dependence of ^{15}N linewidths is partially masked by $^{1}H^{N}$ spin flips resulting in a mixing of TROSY and anti-TROSY relaxation behaviour.

IP-AP crosstalk

Finally, magnetisation modes N_x and $N_xC_z^{\alpha(i)}C_z^{\alpha(i-1)}$ differing in their $^{13}C^{\alpha}$ longitudinal relaxation properties cause (during the variable evolution period t_1) not only differential linewidths within the doublet-of-doublets, but also generate (during the fixed period δ) differential intensities between constituent multiplets, not all of which ascribed to the coherence transfer function (13) alone.

Differential relaxation taking place *during* evolution period t_1 mixes the II and AA constituents mutually, leading in the F_1 dimension to characteristic lineshape twists (Norwood 1993; Harbison 1993; Norwood and Jones 1993; Norwood 1995; Ponstingl and Otting 1998). As $^{13}C^{\alpha}$ longitudinal relaxation properties are identical during both evolution and acquisition periods, the corresponding effect between spin modes H_x^N and $H_x^NC_z^{\alpha(i)}C_z^{\alpha(i-1)}$ is also noticeable in F_2.

The characteristic lineshape twists in an IP doublet arise from mixing *absorptive* in-phase ± *dispersive* anti-phase doublet components ($IP_a \pm x\ AP_d$), and vice versa, when considering an AP signal, from *absorptive* anti-phase ± *dispersive* in-phase components ($AP_a \pm x\ IP_d$). The effect does resemble a first-order phase twist, but contrary to that, the signal is not invariant at its origin and exhibits concave or convex bulging at its center (Fig. 13).

As N_x relaxes slower, and $N_xC_z^{\alpha(i)}C_z^{\alpha(i-1)}$ faster, chiefly during the fixed period δ *prior to* the evolution period t_1, exchange takes place also between components that are separate multiplet constituents in DIPAP spectra, II and AA, respectively. For example, an arbitrary rate differential of $R = 1$ Hz, would yield after $\delta = 50$ ms an intensity ratio of $M_{\mathrm{II}}/M_{\mathrm{AA}} = e^{+\pi\delta R/2}$: $e^{-\pi\delta R/2} = 1.082$: 0.925, that is, some 16% amplitude difference would be anticipated following separation of IP(^{1}J) and AP(^{1}J) terms. The single-$^{13}C^{\alpha}$ spin operators, $N_yC_z^{\alpha(i)}$ or $N_yC_z^{\alpha(i-1)}$ emerge from the other two during the comparatively short period ε, such that the intensities of M_{IA} and M_{AI} are expected to be pairwise similar to M_{II} and M_{AA}, respectively. Generally, amplitude disparity increases with the molecular reorientational correlation time, until pattern II is the only significant component left eventually. In fact, empirical factors of ±8 and ±1% suggest that signal intensities for the investigated samples indeed relate approximately as M_{II}: M_{IA}: M_{AI}: $M_{\mathrm{AA}} = 1.09$: 1.07: 0.93: 0.91.

Robustness and data cross-validation

The simultaneous dependence, in the DIPAP method, of both multiplet amplitudes and splittings on the actual value of J makes the lineshape fit very sensitive by lending the parameter optimization a critical driving force and robustness. By itself, no splitting term changes the amplitude and, conversely, amplitude scaling would not affect the multiplet fine structure. Both normally represent orthogonal parameter types whose effects are separable. A connection between splitting and amplitude is, however, introduced through the transfer function as defined by the fixed parameter δ, which, of course, must be set in the simulation to agree with the experimental value.

Driving force in computer-assisted optimization of IPAP-type spectra is provided by concurrent fitting of pairs of multiplets and by exploiting differing J splitting modulations. Each single subspectrum, in both IPAP and DIPAP spectra, contains all the multiplet information, and each exhibits a different splitting pattern. Obviously, referring to four instead of two data matrices in DIPAP evaluations enhances this driving force due to increased data redundancy, helping determine all coupling parameters with

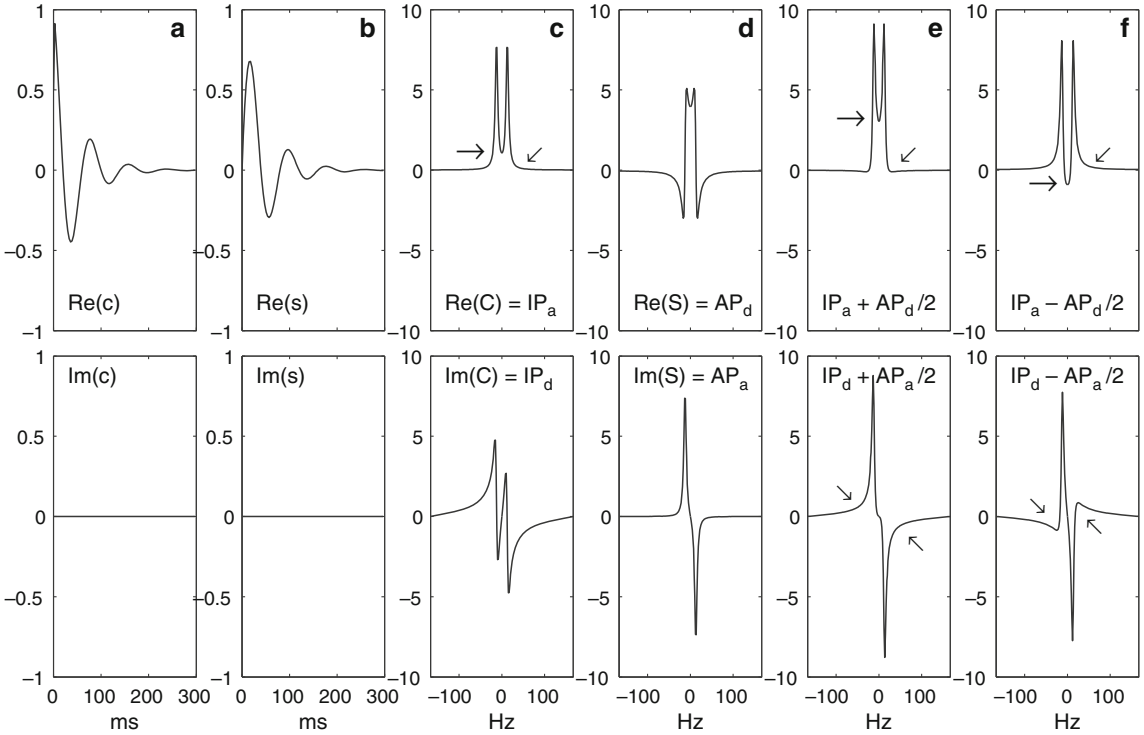

Fig. 13 Demonstration of differential-relaxation effects between IP and AP multiplet constituents (sometimes signified as *J*-crosstalk). Lineshape parameters used are $J = 25$ Hz, $T_2 = 150$ ms, $R_2 = 1/T_2$. **a** Time-domain signals $c(t) = \cos(\pi Jt)\ \exp(-\pi R_2 t)$ and **b** $s(t) = \sin(\pi Jt)\ \exp(-\pi R_2 t)$; **c** Fourier transform of $c(t)$, with *real* and *imaginary* parts yielding *absorptive* and *dispersive* in-phase (IP_a and IP_d) doublet lines; **d** Fourier transform of $s(t)$, with *real* and *imaginary* parts yielding *dispersive* and *absorptive* anti-phase (AP_d and AP_a) doublet lines; **e** arbitrary 2:1 co-addition of *absorptive* in-phase and *dispersive* anti-phase components, resulting in'first-order phase-twisted' doublets; **f** as before but AP inverted, resulting in the opposite phase twist, as seen by the signal tails (*arrows*)

ultimate accuracy and precision. Pearson product-moment correlation coefficients and average discrepancies given in each panel of comparison Fig. 14 indicate high agreement for the large couplings $^2J_{C\alpha N'}$ and $^1J_{N'C\alpha}$. As IPAP spectra are essentially subsets of DIPAP spectra, the variation seen in the values of *J* must therefore be ascribed to the omission of half the experimental data points. Notice that it is impossible to tell from transposable scatter diagrams of the type shown which coupling constants are 'more correct'. Of equal rank, none of the variables is the response of the other, this being a matter of correlation only. With increasing protein size, however, correlation in the small couplings $^2J_{HNC\alpha}$, and $^3J_{C\alpha HN}$ decreases considerably. While variation in the $^3J_{C\alpha HN}$ couplings appears to be purely random, the tilted regression lines seen in the $^2J_{HNC\alpha}$ panels suggest that data spreads are smaller in the DIPAP than in the reference-IPAP sets. The xylanase sample used was considerably less concentrated than the samples of ubiquitin and RNase T1, implying a higher noise level and consequently more randomness in the xylanase data and also in the respective correlation diagrams.

The presence of multiple DIPAP constituents permits straightforward cross-validation of the results obtained. Ideally, *J* coupling averages and standard deviations (spreads within a spectral set) should emerge identically from evaluating either pair of DIPAP constituent multiplets separately and independently. Any systematic variation would be a consequence of omitting half the available data. Eventually, fitting all DIPAP patterns concomittantly should be most reliable, its outcome somewhat representing the average over the six possible pair evaluations, results of which are compiled for ubiquitin in Table 2.

Interestingly, the original IPAP scheme by Permi and Annila (2000) reproduces closely the $^2J_{C\alpha N'}$ and $^1J_{N'C\alpha}$ coupling constants obtained with our DIPAP scheme. This is likely a consequence of its data pair comprising the two-constituent subset, II/IA, that exhibits the smallest ($n = 0$) and largest ($n = 3$) number of signal nodes, respectively. Similarly, the complementary subset AI/AA ($n = 1,2$), exhibiting ^1J as antiphase rather than inphase splitting, also produces satisfactory $^2J_{C\alpha N'}$ and $^1J_{N'C\alpha}$ coupling constants, if slightly larger by 0.1 Hz on average. Disparate results emerge, however, when combining any other pair, where the symmetrical II/AA ($n = 0,2$) and antisymmetrical IA/AI ($n = 3,1$) pattern pairings fare as poorly as the remaining combinations of odd or even symmetry features, II/AI

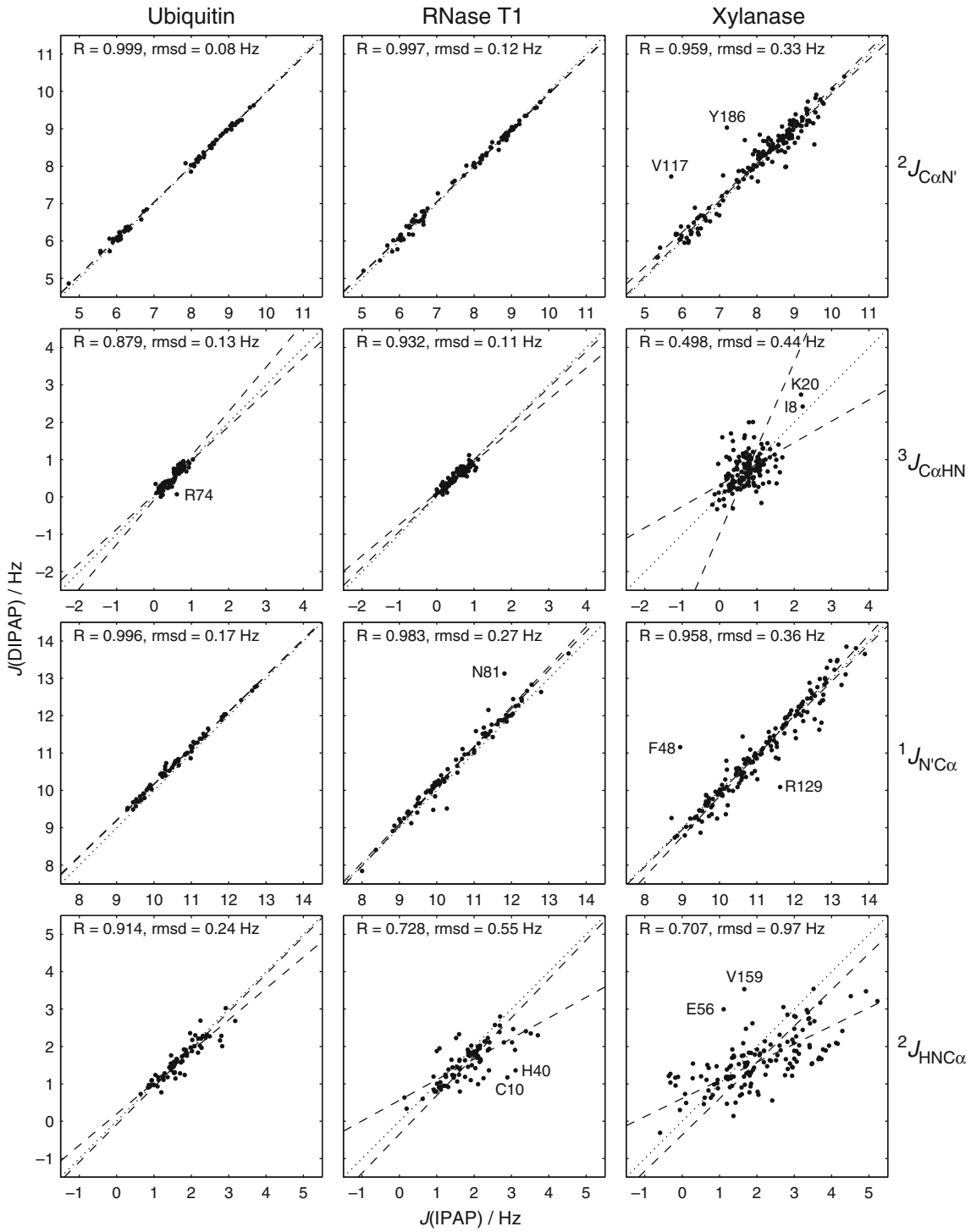

($n = 0,1$) and IA/AA ($n = 3,2$). Between the latter subsets, the mean couplings $^2J_{C\alpha N'}$ and $^1J_{N'C\alpha}$ deviate toward opposite directions, differing by as much as 0.6–0.7 Hz between the pairs, and by up to 0.3–0.5 Hz from the DIPAP values, clearly above measurement standard error.

Similar effects are observed for the small coupling constants $^3J_{C\alpha HN}$ and $^2J_{HNC\alpha}$. Most notably, the original IPAP scheme (II/IA pair) appears to produce the largest average values of $^2J_{HNC\alpha}$, and the complementary AI/AA set the smallest, possibly a consequence of $C^{\alpha(i)}$-related

◀ **Fig. 14** Comparison of coupling constants from DIPAP and standard IPAP spectra. Larger discrepancies between IPAP and DIPAP derived couplings resulted in the outliers identified and were explained as follows. The ubiquitin R74 multiplet suffers from particularly poor S/N, apparently due to unlucky interference between conformational exchange timescales in this and adjacent residues (Schneider et al. 1992) and the rates of amide hydrogen exchange caused by the conditions in the low-conductivity HEPES buffer used (Kelly et al. 2002). Multiplets N81 and C10 in RNase T1 are both affected by overlap from other signals affecting F_1 and F_2 related parameters, respectively (see Supplementary Material). Other outliers fall into one of those categories. Similar to the N81 case, xylanase V117 overlaps with I29 and both can only be separated in DIPAP evaluations (Supplementary Material). The xylanase I8 multiplet is surrounded by Y14, L92, and I201. Signals xylanase Y186 and R129 as well as RNase H40 resemble the C10 case. Xylanase signals K20, F48, E56, V159, and Y186 are weak multiplets of poor S/N. The details indicate that the DIPAP data can be fitted more robustly under adverse conditions, and this is where accuracy arises which, however, cannot manifest in a scattergram

differential relaxation inflicted on the antiphase but not on the inphase $^{1}J_{\mathrm{N'C\alpha}}$ splitting.

Reproducibility of $^{3}J_{\mathrm{C\alpha HN}}$ and $^{2}J_{\mathrm{HNC\alpha}}$ coupling constants seems particularly low with the exclusively symmetrical II/AA pairing. As linewidths become broader and differences between the large couplings smaller, the inner line pair in some of the doublet-of-doublets coalesces, while both patterns lack an anti-symmetrical counterpart in order for the splittings to be disentangled adequately.

Together, the two E.COSY tilts ($^{1}J_{\mathrm{N'C\alpha}}/^{2}J_{\mathrm{HNC\alpha}}$ and $^{2}J_{\mathrm{C\alpha N'}}/^{3}J_{\mathrm{C\alpha HN}}$) impose upper limits on the 2D multiplet extent and, thus, on the sum of the respective couplings in both F_1 and F_2 dimensions. Table 2 shows how these are being reproduced for the different pair combinations.

Special case: ^{1}J and ^{2}J of similar size

The DIPAP pattern for Ser13 in RNase T1 suggests that the value of $^{2}J_{\mathrm{C\alpha N'}}$ (8.53 Hz) exceeds that of $^{1}J_{\mathrm{N'C\alpha}}$ (7.98 Hz), a fact impossible to fathom with, e.g., *J*-modulation methods. This was corroborated by comparing in an HNCA spectrum (Ikura et al. 1990) the respective peak intensities reflecting magnetization transmitted through ^{1}J and ^{2}J also, yet manifest as two separate correlation signals. Indeed, the *inter*-residual Ser12/Ser13 correlation appears slightly stronger than the *intra*-residual Ser13 signal. The ^{2}J coupling can be independently retrieved from C^{α}-coupled HNCO (Puttonen et al. 2006; Kazimierczuk et al. 2008), not however the ^{1}J coupling.

According to data deposited in BMRB-16580 (Schmidt et al. 2010) and BMRB-15905 (Schmidt et al. 2009), originating from a variety of 2D and 3D NMR methods, $^{2}J_{\mathrm{C\alpha N'}}$ is 8.20 Hz in Ser12, and $^{1}J_{\mathrm{N'C\alpha}}$ is 8.67 Hz in Ser13. A large $^{2}J_{\mathrm{C\alpha N'}}$ coupling for the preceding residue *i*–1 in conjunction with a small $^{1}J_{\mathrm{N'C\alpha}}$ coupling for the current residue *i* appears to indicate α-helix initiation, especially if $^{2}J_{\mathrm{C\alpha N'}}$ in the current residue *i* is small also (Schmidt et al. 2011). This is truly the case for RNase T1, where 4.50 Hz for $^{2}J_{\mathrm{C\alpha N'}}$ in Ser13, as measured in the Ser14 multiplet, marks the beginning of the sole α-helix present in the enzyme (Hoffmann and Rüterjans 1988).

Asn42 in xylanase (Fig. 7) appears as another pattern in which ^{2}J exceeds ^{1}J. However, comparison with $^{1}J_{\mathrm{N'C\alpha}}$ and $^{2}J_{\mathrm{C\alpha N'}}$ data previously obtained for xylanase using quantitative *J*-correlated [^{15}N,^{1}H]-TROSY-HNC (Wienk et al. 2003) was impossible as reference values for both $^{2}J_{\mathrm{C\alpha N'}}$ in Asn41 and $^{1}J_{\mathrm{N'C\alpha}}$ in Asn42 are missing from the dataset because of low signal amplitudes. Depositions BMRB-16583 and BMRB-15908, respectively, quote averages of 8.59 and 9.35 Hz for $^{2}J_{\mathrm{C\alpha N'}}$ and $^{1}J_{\mathrm{N'C\alpha}}$ in Asn41 and Asn42. But then, at 7.11 Hz, the subsequent $^{2}J_{\mathrm{C\alpha N'}}$ value in Asn42 is too large to suggest α-helix initiation. The similar values of ^{2}J and ^{1}J in xylanase are due to an isolated set of *left-handed helix-like positive* ϕ and ψ torsion angles in Asn42 only. X-ray data (PDB-1QH7; Sabini et al. 1999) hint at a γ turn motif.

Table 2 Cross-validation of DIPAP results by independent fitting of subspectrum pairs and omission of the remaining pairs

Constituents	Nodes	F_1			F_2		
		$^{1}J_{\mathrm{N'C\alpha}}$	$^{2}J_{\mathrm{C\alpha N'}}$	Σ*J*	$^{2}J_{\mathrm{HNC\alpha}}$	$^{3}J_{\mathrm{C\alpha HN}}$	Σ*J*
II + IA	(0,3)	10.77 ± 0.83 ± 0.03	7.64 ± 1.31 ± 0.07	18.41	1.95 ± 0.60 ± 0.09	0.60 ± 0.32 ± 0.09	2.55
II + AI	(0,1)	10.22 ± 1.05 ± 0.21	7.88 ± 1.34 ± 0.19	18.10	1.73 ± 0.53 ± 0.10	0.71 ± 0.61 ± 0.30	2.44
II + AA	(0,2)	11.05 ± 0.84 ± 0.10	7.24 ± 1.17 ± 0.07	18.29	1.90 ± 0.70 ± 0.42	0.63 ± 0.53 ± 0.38	2.53
IA + AI	(3,1)	10.64 ± 0.89 ± 0.07	8.16 ± 1.16 ± 0.06	18.80	1.72 ± 0.55 ± 0.11	0.63 ± 0.34 ± 0.15	2.35
IA + AA	(3,2)	10.90 ± 0.86 ± 0.10	7.26 ± 1.48 ± 0.41	18.16	1.86 ± 0.65 ± 0.10	0.42 ± 0.29 ± 0.09	2.28
AI + AA	(1,2)	10.87 ± 0.85 ± 0.13	7.73 ± 1.23 ± 0.06	18.60	1.68 ± 0.59 ± 0.10	0.59 ± 0.35 ± 0.12	2.27
DIPAP (all)	(0,1,2,3)	10.78 ± 0.90 ± 0.05	7.57 ± 1.33 ± 0.03	18.35	1.83 ± 0.58 ± 0.08	0.62 ± 0.29 ± 0.08	2.45

Averages (in Hz) from 68 ubiquitin signals recorded at 950 MHz, using three DIPAP experiments (without BIRD module) with δ periods of 44, 50, and 56 ms. Mean values are reported with standard deviation and standard error, i.e., *intra*-spectrum variation, reflecting conformational diversity across the amino-acid residues, and *inter*-spectrum variation, indicating experimental reproducibility

The α-helix initiation at Ile23 in ubiquitin could not be traced in the present data as the respective $^{2}J_{C\alpha N'}$ would need to be measured in the Glu24 multiplet which is notoriously absent from all spectra.

Any ambiguity arising in the measurement of residual dipolar coupling (RDC) (Ottiger et al. 1998) from the possible situation in which $(^{1}J + {}^{1}D) < (^{2}J + {}^{2}D)$ should be readily resolvable by using the DIPAP method.

Conclusions

Different combinations of four subspectra of a dataset result in the selective elimination of individual splittings and have previously helped simplify spectra for detailed analysis (Kontaxis and Bax 2001; Duma et al. 2003). Other applications using a combination of four subspectra typically have a DIPAP pulse-sequence module inserted immediately prior to the data acquisition period in order to afford the 'virtual decoupling' of selected interactions, e.g., in homonuclear ^{13}C,^{13}C-correlation spectroscopy (Bermel et al. 2006).

Like previous methods, our DIPAP approach seeks to increase robustness in parameter extraction by exploiting overdetermination at the *effect* level, that is, by simultaneously evaluating different multiplets that share several model parameters but differ in one modulation mode. Most prevalent in homonuclear COSY type spectroscopy of spin systems with three or more coupled spins, the roles of active and passive couplings and, thus, inphase and antiphase splitting patterns alternate between different cross peaks belonging to the same spin system. This effect providing parameter overdetermination within a single spectral record was exploited for the accurate determination of homonuclear coupling constants (Schmidt 1998). In the present case of heteronuclear DIPAP spectroscopy, multiplets are merely separated into individual spectral records but nevertheless evaluated simultaneously.

Multiplets composed of multiple splittings, on principle, allow one pair of independent inphase/antiphase subspectra to be recorded for each doublet. By combining the total 2^N subspectra, all N contributing J-coupling constants would be extracted unambiguously by forming various sums and differences of spectrum traces (Oschkinat and Freeman 1984). Our DIPAP approach follows this same idea.

Acknowledgments We thank Bernhard Brutscher, Norman Spitzner, and Marco Betz for providing samples of ubiquitin, RNase T1, and xylanase, respectively. Financial support by the Access to Research Infrastructures activity in the 7th Framework Programme of the EC (Project number: 261863, Bio-NMR) for conducting the research is gratefully acknowledged.

References

Bermel W, Bertini I, Felli IC, Piccioli M, Pierattelli R (2006) ^{13}C-detected protonless NMR spectroscopy of proteins in solution. Prog NMR Spectrosc 48:25–45

Betz M, Löhr F, Wienk H, Rüterjans H (2002) Letter to the Editor: ^{1}H, ^{13}C and ^{15}N chemical shift assignment of *Bacillus agaradhaerens* family 11 xylanase. J Biomol NMR 23:333–334

Boisbouvier J, Bax A (2002) Long-range magnetization transfer between uncoupled nuclei by dipole-dipole cross-correlated relaxation: a precise probe of β-sheet geometry in proteins. J Am Chem Soc 124:11038–11045

Bracewell RN (1986) The Fourier transform and its applications, 2nd Intl Edn. McGraw-Hill, New York

Brutscher B (2002) Intraresidue HNCA and COHNCA experiments for protein backbone resonance assignment. J Magn Reson 156:155–159

Daragan VA, Mayo KH (1997) Motional model analyses of protein and peptide dynamics using ^{13}C and ^{15}N NMR relaxation. Prog NMR Spectrosc 31:63–105

Delaglio F, Torchia DA, Bax A (1991) Measurement of ^{15}N–^{13}C *J* couplings in staphylococcal nuclease. J Biomol NMR 1:439–446

Duma L, Hediger S, Lesage A, Emsley L (2003) Spin-state selection in solid-state NMR. J Magn Reson 164:187–195

Edison AS, Markley JL, Weinhold F (1994a) Calculations of one-, two- and three-bond nuclear spin-spin couplings in a model peptide and correlations with experimental data. J Biomol NMR 4:519–542

Edison AS, Weinhold F, Westler WM, Markley JL (1994b) Estimates of ϕ and ψ torsion angles from one-, two- and three-bond nuclear spin-spin couplings: application to staphylococcal nuclease. J Biomol NMR 4:543–551

Emetarom C, Hwang T-L, Mackin G, Shaka AJ (1995) Isotope editing of NMR spectra. Excitation sculpting using BIRD pulses. J Magn Reson A 115:137–140

Engelke J, Rüterjans H (1995) Determination of $^{13}C^{\alpha}$ relaxation times in uniformly ^{13}C/^{15}N-enriched proteins. J Biomol NMR 5:173–182

Favier A, Brutscher B (2011) Recovering lost magnetization: polarization enhancement in biomolecular NMR. J Biomol NMR 49:9–15

Fushman D, Cowburn D (2001) Nuclear magnetic resonance relaxation in determination of residue-specific ^{15}N chemical shift tensors in proteins in solution: protein dynamics, structure, and applications of transverse relaxation optimized spectroscopy. Meth Enzymol 339:109–126

Fushman D, Weisemann R, Thüring H, Rüterjans H (1994) Backbone dynamics of ribonuclease T1 and its complex with 2′GMP studied by two-dimensional heteronuclear NMR spectroscopy. J Biomol NMR 4:61–78

Garbow JR, Weitekamp DP, Pines A (1982) Bilinear rotation decoupling of homonuclear scalar interactions. Chem Phys Lett 93:504–509

Geen H, Freeman R (1991) Band-selective radiofrequency pulses. J Magn Reson 93:93–141

Griesinger C, Sørensen OW, Ernst RR (1987) Practical aspects of the E. COSY technique. Measurement of scalar spin-spin coupling constants in peptides. J Magn Reson 75:474–492

Grzesiek S, Bax A (1993a) The importance of not saturating H_2O in protein NMR. Application to sensitivity enhancement and NOE measurements. J Am Chem Soc 115:12593–12594

Grzesiek S, Bax A (1993b) Amino acid type determination in the sequential assignment procedure of uniformly ^{13}C/^{15}N-enriched proteins. J Biomol NMR 3:185–204

Guo C, Godoy-Ruiz R, Tugarinov V (2010) High resolution measurement of methyl $^{13}C_m$–^{13}C and $^{1}H_m$–$^{13}C_m$ residual dipolar couplings in large proteins. J Am Chem Soc 132:13984–13987

Harbison GS (1993) Interference between *J*-couplings and cross-relaxation in solution NMR spectroscopy: consequences for macromolecular structure determination. J Am Chem Soc 115:3026–3027

Hoffmann E, Rüterjans H (1988) Two-dimensional ^{1}H-NMR investigation of ribonuclease T1—resonance assignments, secondary structure and low-resolution tertiary structure of ribonuclease T1. Eur J Biochem 177:539–560

Ikura M, Kay LE, Bax A (1990) A novel approach for sequential assignment of proton, carbon-13, and nitrogen-15 spectra of larger proteins: heteronuclear triple-resonance three-dimensional NMR spectroscopy. Application to calmodulin. Biochemistry 29:4659–4667

Kay LE, Ikura M, Tschudin R, Bax A (1990) Three-dimensional triple-resonance NMR spectroscopy of isotopically enriched proteins. J Magn Reson 89:496–514

Kazimierczuk K, Zawadzka A, Koźmiński W, Zhukov I (2008) Determination of spin-spin couplings from ultrahigh resolution 3D NMR spectra obtained by optimized random sampling and multidimensional Fourier transformation. J Am Chem Soc 130:5404–5405

Kelly AE, Ou HD, Withers R, Dötsch V (2002) Low-conductivity buffers for high-sensitivity NMR measurements. J Am Chem Soc 124:12013–12019

Kontaxis G, Bax A (2001) Multiplet component separation for measurement of methyl ^{13}C–^{1}H dipolar couplings in weakly aligned proteins. J Biomol NMR 20:77–82

Kövér KE, Batta G (2004) More line narrowing in TROSY by decoupling of long-range couplings: shift correlation and $^{1}J_{NC'}$ coupling constant measurements. J Magn Reson 170:184–190

Kuboniwa H, Grzesiek S, Delaglio F, Bax A (1994) Measurement of H^N, H^α *J*-couplings in calcium-free calmodulin using new 2D and 3D water-flip-back methods. J Biomol NMR 4:871–878

Kumar A, Christy Rani Grace R, Madhu PK (2000) Cross-correlations in NMR. Prog NMR Spectrosc 37:191–319

Kupče É, Freeman R (1994) Wide-band excitation with polychromatic pulses. J Magn Reson A 108:268–273

Kupče É, Freeman R (1995) Adiabatic pulses for wideband inversion and broadband decoupling. J Magn Reson A 115:273–276

Lee D, Hilty C, Wider G, Wüthrich K (2006) Effective rotational correlation times of proteins from NMR relaxation interference. J Magn Reson 178:72–76

Lescop E, Kern T, Brutscher B (2010) Guidelines for the use of band-selective radiofrequency pulses in hetero-nuclear NMR: example of longitudinal-relaxation-enhanced BEST-type H-1-N-15 correlation experiments. J Magn Reson 203:190–198

Liu Y, Prestegard JH (2009) Measurement of one and two bond N–C couplings in large proteins by TROSY-based *J*-modulation experiments. J Magn Reson 200:109–118

Logan M, Olejniczak ET, Xu RX, Fesik SW (1992) Side chain and backbone assignments in isotopically labeled proteins from two heteronuclear triple resonance experiments. FEBS Lett 314:413–418

Löhr F, Pérez C, Köhler R, Rüterjans H, Schmidt JM (2000) Heteronuclear relayed E.COSY revisited: determination of $^{3}J(H^\alpha,C^\gamma)$ couplings in Asx and aromatic residues in proteins. J Biomol NMR 18:13–22

Matsuo H, Kupče É, Li H, Wagner G (1996) Use of selective Cα pulses for improvement of HN(CA)CO-D and HN(COCA)NH-D experiments. J Magn Reson B 111:194–198

Nietlispach D, Ito Y, Laue ED (2002) A novel approach for the sequential backbone assignment of larger proteins: selective intra-HNCA and DQ-HNCA. J Am Chem Soc 124:11199–11207

Norwood TJ (1993) Measurement of the scalar coupling and transverse relaxation times of doublets. J Magn Reson A 101: 109–112

Norwood TJ (1995) The effects of relaxation on the E.COSY experiment. J Magn Reson A 114:92–97

Norwood TJ, Jones K (1993) Relaxation effects and the measurement of scalar coupling constants using the E.COSY experiment. J Magn Reson A 104:106–110

Oschkinat H, Freeman R (1984) Fine structure in two-dimensional NMR correlation spectroscopy. J Magn Reson 60:164–169

Ottiger M, Bax A (1998) Determination of relative N–HN, N–C', Cα–C' and Cα–Hα effective bond lengths in a protein by NMR in a dilute liquid crystalline phase. J Am Chem Soc 120:12334–12341

Ottiger M, Delaglio F, Bax A (1998) Measurement of *J* and dipolar couplings from simplified two-dimensional NMR spectra. J Magn Reson 131:373–378

Permi P (2002) Intraresidual HNCA: an experiment for correlating only intraresidual backbone resonances. J Biomol NMR 23:201–209

Permi P, Annila A (2000) Transverse relaxation optimised spin-state selective NMR experiments for measurement of residual dipolar couplings. J Biomol NMR 16:221–227

Pervushin K (2000) Impact of transverse relaxation optimized spectroscopy (TROSY) on NMR as a technique in structural biology. Q Rev Biophys 33:161–197

Pervushin K, Riek R, Wider G, Wüthrich K (1997) Attenuated T_2 relaxation by mutual cancellation of dipole–dipole coupling and chemical shift anisotropy indicates an avenue to NMR structures of very large biological macromolecules in solution. Proc Natl Acad Sci USA 94:12366–12371

Pervushin KV, Wider G, Wüthrich K (1998) Single transition-to-single transition polarization transfer (ST2-PT) in [^{15}N,^{1}H]-TROSY. J Biomol NMR 12:345–348

Ponstingl H, Otting G (1998) Rapid measurement of scalar three-bond $^{1}H^N$–$^{1}H^\alpha$ spin coupling constants in ^{15}N-labelled proteins. J Biomol NMR 12:319–324

Puttonen E, Tossavainen H, Permi P (2006) Simultaneous determination of one- and two-bond scalar and residual dipolar couplings between $^{13}C'$, $^{13}C\alpha$, and ^{15}N spins in proteins. Magn Reson Chem 44:168–176

Sabini E, Sulzenbacher G, Dauter M, Dauter Z, Jørgensen PL, Schülein M, Dupont C, Davies GJ, Wilson KS (1999) Catalysis and specificity in enzymatic glycoside hydrolysis: a 2,5B conformation for the glycosyl-enzyme intermediate revealed by the structure of the *Bacillus agaradhaerens* family 11 xylanase. Chem Biol 6:483–492

Schanda P, Van Melckebeke H, Brutscher B (2006) Speeding up three-dimensional protein NMR experiments to a few minutes. J Am Chem Soc 128:9042–9043

Schmidt JM (1997) Conformational equilibria in polypeptides. I. determination of accurate $^{3}J_{HC}$ coupling constants in antamanide by 2D NMR multiplet simulation. J Magn Reson 124:298–309

Schmidt JM (1998) Double-quantum-filtered COSY simulation applied to least-squares regression of J_{HH} coupling constants. Mol Phys 95:809–826

Schmidt JM, Howard MJ, Maestre-Martínez M, Pérez CS, Löhr F (2009) Variation in protein C^α-related one-bond *J* couplings. Magn Reson Chem 47:16–30

Schmidt JM, Hua Y, Löhr F (2010) Correlation of ^{2}J couplings with protein secondary structure. Proteins 78:1544–1562

Schmidt JM, Zhou S, Rowe ML, Howard MJ, Williamson RA, Löhr F (2011) One-bond and two-bond *J* couplings help annotate protein secondary-structure motifs: *J*-coupling indexing applied to human endoplasmic reticulum protein ERp18. Proteins 79: 428–443

Schneider DM, Dellwo MJ, Wand AJ (1992) Fast internal main-chain dynamics of human ubiquitin. Biochemistry 31:3645–3652

Schuldiner M, Metz J, Schmid V, Denic V, Rakwalska M, Schmitt HD, Schwappach B, Weissman JS (2008) The GET complex mediates insertion of tail-anchored proteins into the ER membrane. Cell 134:634–645

Schwarz D, Junge F, Durst F, Frölich N, Schneider B, Reckel S, Sobhanifar S, Dötsch V, Bernhard F (2007) Preparative scale expression of membrane proteins in *Escherichia coli*-based continuous exchange cell-free systems. Nat Protoc 2:2945–2957

Spitzner N, Löhr F, Pfeiffer S, Koumanov A, Karshikov A, Rüterjans H (2001) Ionization properties of titratable groups in ribonuclease T1—pK_a values in the native state determined by two-dimensional heteronuclear NMR spectroscopy. Eur J Biochem 30:186–195

Stonehouse J, Shaw GL, Keeler J, Laue ED (1994) Minimizing sensitivity losses in gradient-selected ^{15}N–^{1}H HSQC spectra of proteins. J Magn Reson A 107:178–184

Uhrín D, Liptaj T, Kövér KE (1993) Modified BIRD pulses and design of heteronuclear pulse sequences. J Magn Reson A 101:41–46

Vuister GW, Bax A (1993) Quantitative *J* correlation: a new approach for measuring homonuclear three-bond $J(H^NH^\alpha)$ coupling constants in ^{15}N-enriched proteins. J Am Chem Soc 115:7772–7777

Wand AJ, Urbauer JL, McEvoy RP, Bieber RJ (1996) Internal dynamics of human ubiquitin revealed by ^{13}C-relaxation studies of randomly fractionally labeled protein. Biochemistry 35:6116–6125

Wienk HLJ, Martínez MM, Yalloway GN, Schmidt JM, Pérez C, Rüterjans H, Löhr F (2003) Simultaneous measurement of protein one-bond and two-bond nitrogen-carbon coupling constants using an internally referenced quantitative J-correlated [^{15}N,^{1}H]-TROSY-HNC experiment. J Biomol NMR 25:133–145

Wirmer J, Schwalbe H (2002) Angular dependence of $^{1}J(N_i, C_i^\alpha)$ and $^{2}J(N_i, C_{(i-1)}^\alpha)$ coupling constants measured in J-modulated HSQCs. J Biomol NMR 23:47–55

Yao L, Ying J, Bax A (2009) Improved accuracy of ^{15}N–^{1}H scalar and residual dipolar couplings from gradient-enhanced IPAP-HSQC experiments on protonated proteins. J Biomol NMR 43:161–170

Yao L, Grishaev A, Cornilescu G, Bax A (2010a) Site-specific backbone amide on amide ^{15}N chemical shift anisotropy in a small protein from liquid crystal and cross-correlated relaxation measurements. J Am Chem Soc 132:4295–4309

Yao L, Grishaev A, Cornilescu G, Bax A (2010b) The impact of hydrogen bonding on amide ^{1}H chemical shift anisotropy studied by cross-correlated relaxation and liquid crystal NMR spectroscopy. J Am Chem Soc 132:10866–10875